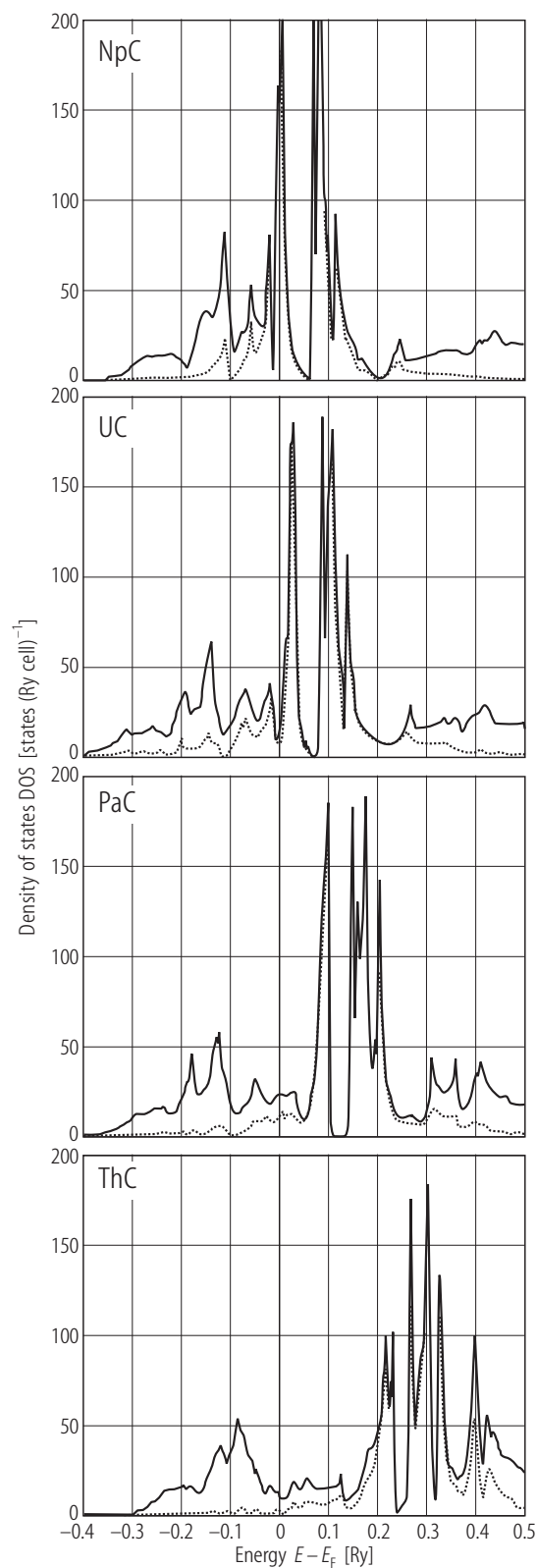


## I. AnC. Actinide monocarbides



←

**Fig. I.1.** AnC (An = Th...Np). Electronic structure of the actinide monocarbides. DOS calculated with a relativistic APW method and LDA [90HY2]. The solid and dashed curves show the total and the 5f band DOS, respectively. The 6p bands of the actinides and the C 2s bands lie below  $-0.4$  Ry. The occupation of the 5f electrons increases with increasing  $Z$  number of actinide content. DOS at  $E_F$  is 15, 24, 28 and 121 states/Ry cell, for ThC, PaC, UC and NpC, respectively.

**Fig. I.2.** AnC (An = Th...Np). Self-consistent energy band structures along [100] and [111] calculated by RKKR method using  $X_\alpha$  exchange parameters [82M]. Note that the dispersion of the  $\Delta_7$  band, which intersects the carbon p-like band near X point is continuously decreased with increasing  $Z$  of the metal constituents. If in ThC the dispersion of this band is typically d-like, then in NpC the  $\Delta_7$  band is well localized. Although the s-p-d partial charges do not vary greatly across the series, the  $f_{7/2}$  and particularly  $f_{5/2}$  increase dramatically with  $Z$ . For details such as  $\gamma$ -like partial radial charges (Fig. I.3), the total charges, charge transfer and Fermi energies for this series of AnC carbides see the original paper [82M] and a summary given in [87WG].

For Fig. I.2 see next page

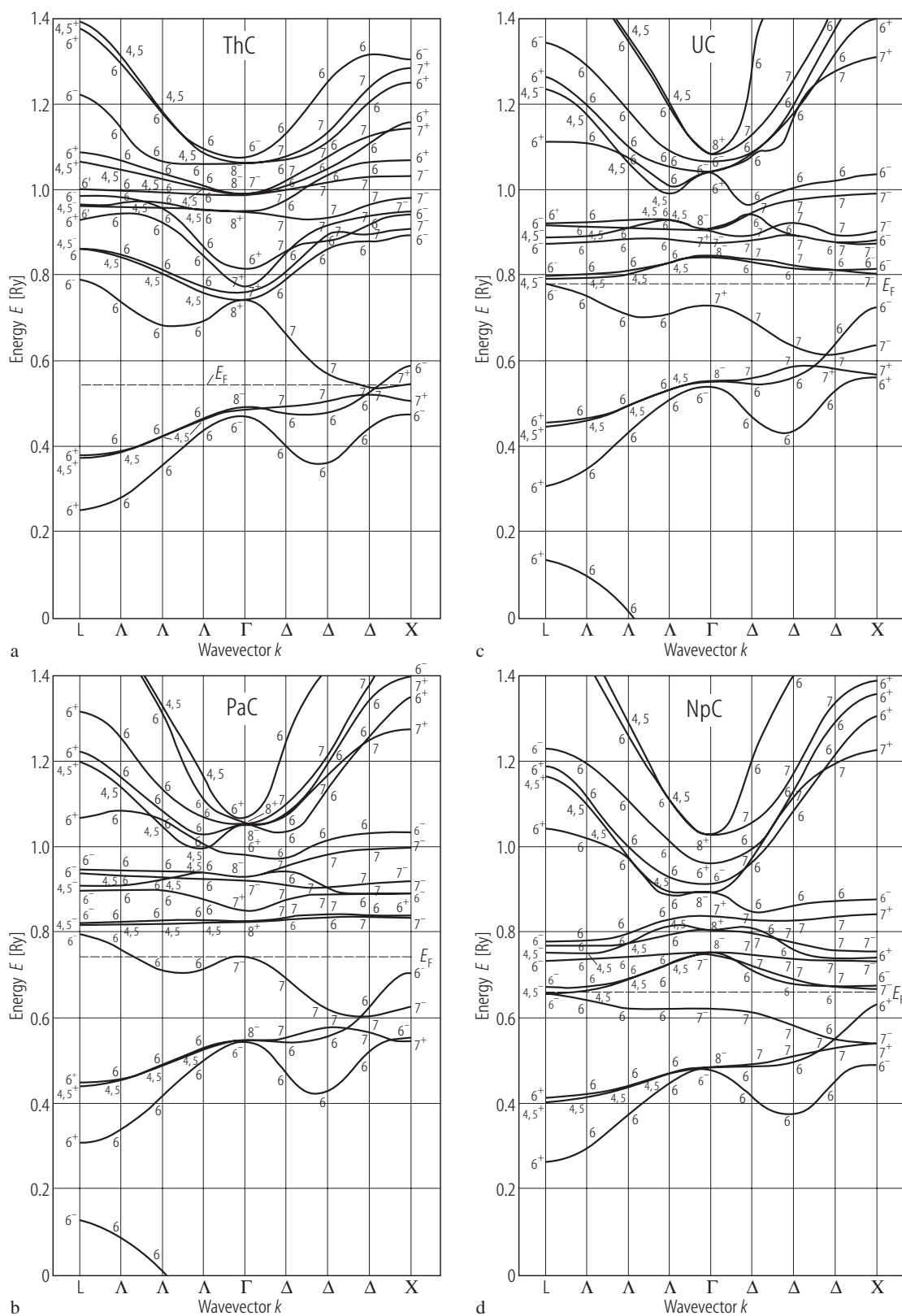
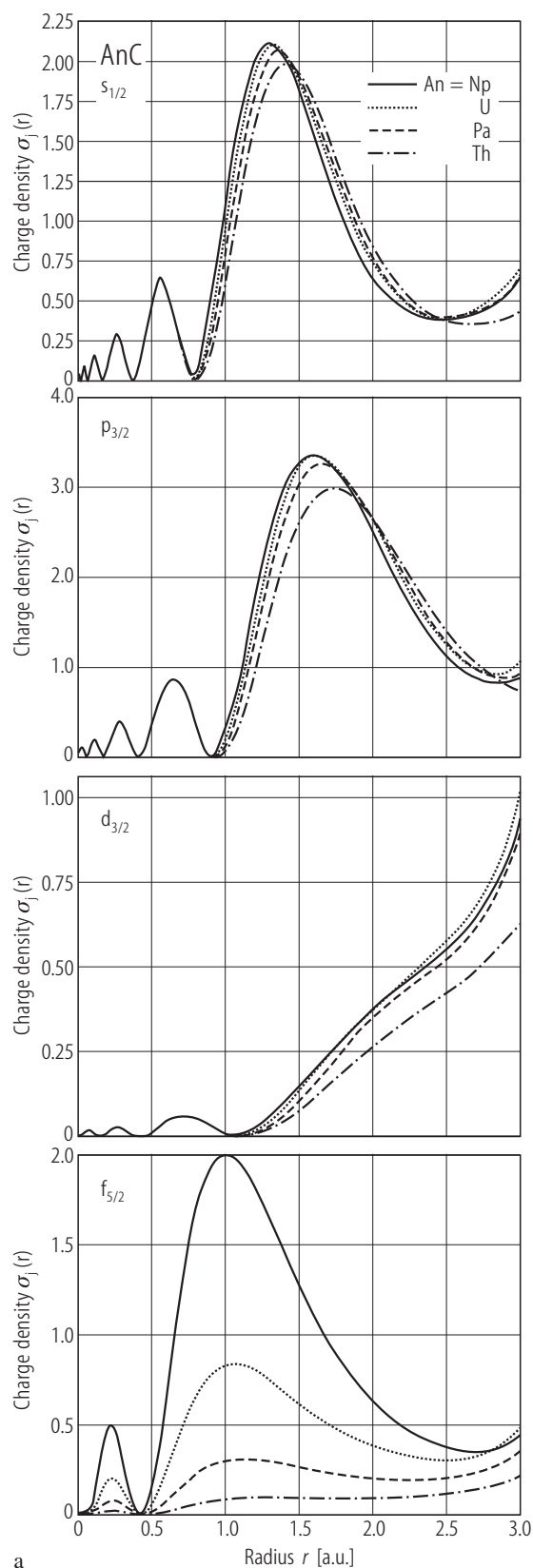
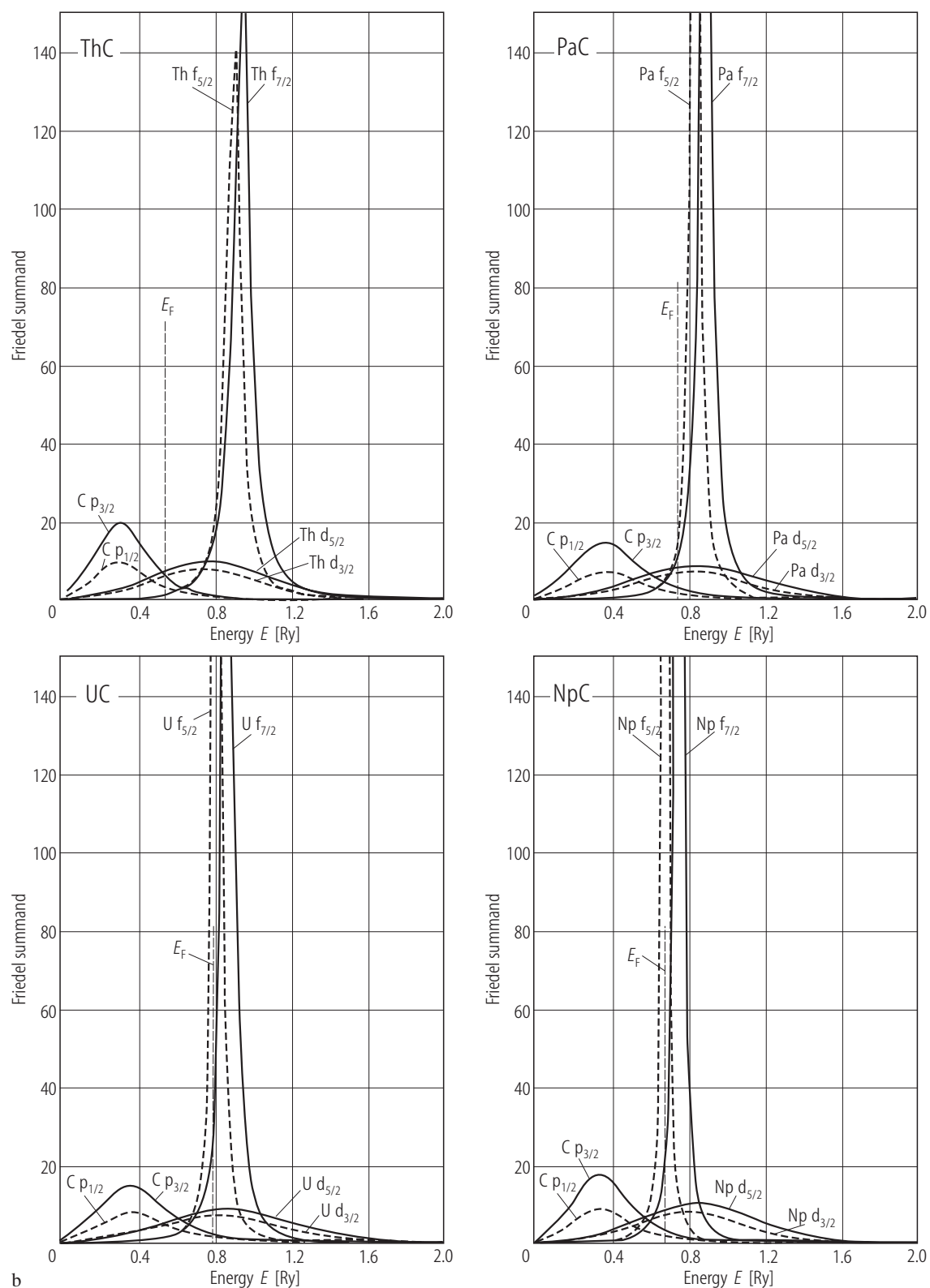


Fig. I.2. For caption see previous page



**Fig. 1.3.** AnC (An = Th, Pa, U, Np). **(a)** The individual radial charge densities  $\sigma_j(r)$  within the metal spheres for  $s_{1/2}$ ,  $p_{3/2}$ ,  $d_{3/2}$  and  $f_{5/2}$  components [82M]. Note that only the metal f-electron curves show striking difference in passing across the series. **(b)** The single-site differential Friedel sums for resonant partial curves of each atomic constituent [82M]. All the carbon curves are similar in the size shape and position. Note that the strongly resonant f bands decrease in energy and in width on going from Th to Np, and the region below  $E_F$  becomes a more f-electron character.

For Fig. 1.3 (b) see next page

**Fig. I.3 (b).** For caption see previous page.

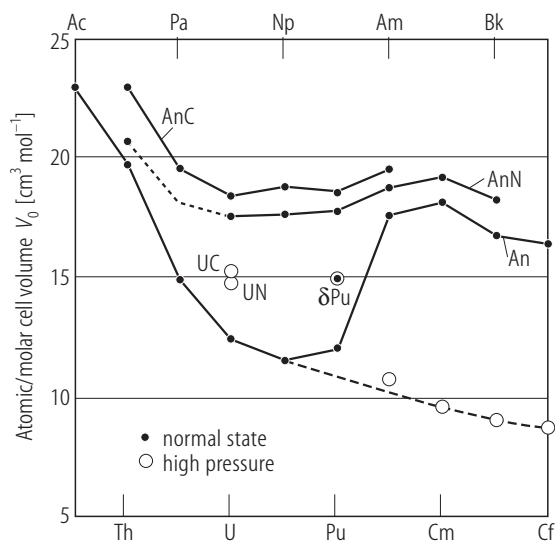


**Fig. I.4.** AnC, AnN. Atomic/molar cell volumes  $V_0$  of the actinide metals (An), monocarbides (AnC) and mononitrides (AnN) in the normal state and under high pressure as a function of actinide element [87I]. Lattice parameters of actinide monocarbides are given in Table I [87B]. The isomorphism of all the actinide monocarbides (all crystallize in the NaCl ( $B_1$ )-type structure) allows one to visualize the bond length variation simply in terms of the lattice parameters. As is the case of actinide metals from Pa to Pu, also for their monocarbides the bond shortening occurs. For comparison the data for the regular  $\delta$ -Pu-phase are also given.

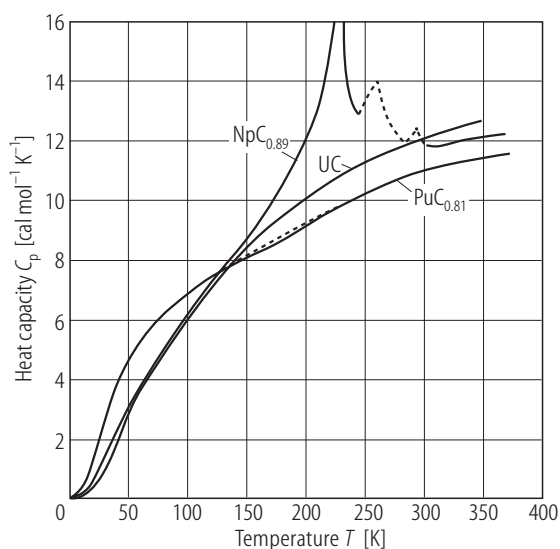


**Fig. I.7.** AnC (An = U, Pu, Np). Heat capacity,  $C_p$ , vs. temperature,  $T$ , up to 350 K [70SG].

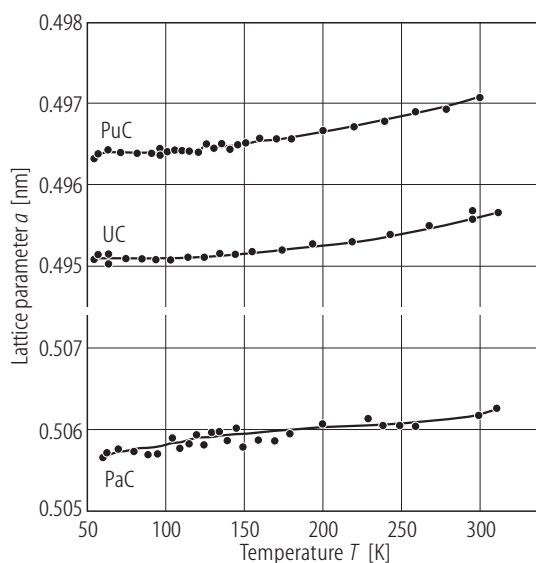


**Fig. I.5.** AnC (An = Pa, U, Pu). The lattice parameter,  $a$ , vs. temperature,  $T$ , for PaC, UC and PuC [79BDM].

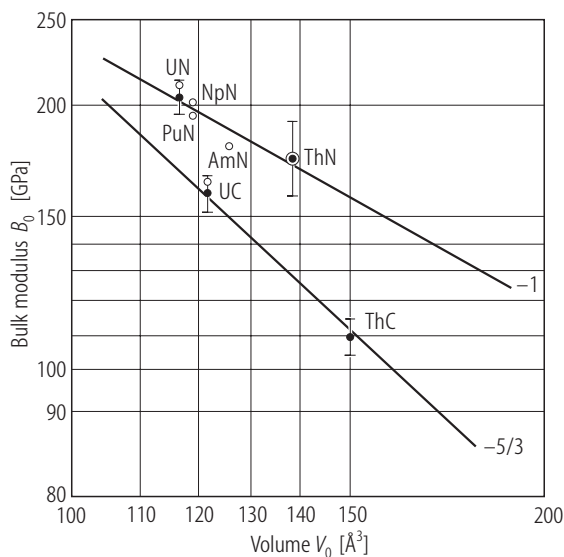


**Fig. I.6.** AnC, AnN. A log - log plot of bulk modulus  $B_0$  vs. volume  $V_0$  for actinide monocarbides and nitrides [90GSBL]. Closed circles are experimental results of [86GSBI], [86SSGB] and [90GSBL]. Open circles are theoretical values of [84B1-3]. Note that the carbides and nitrides have a different  $B_0$  vs.  $V_0$ -scaling. The slope of -1 for the nitrides indicates their predominant ionic character, according with conclusions of theoretical calculations [84B1-3].

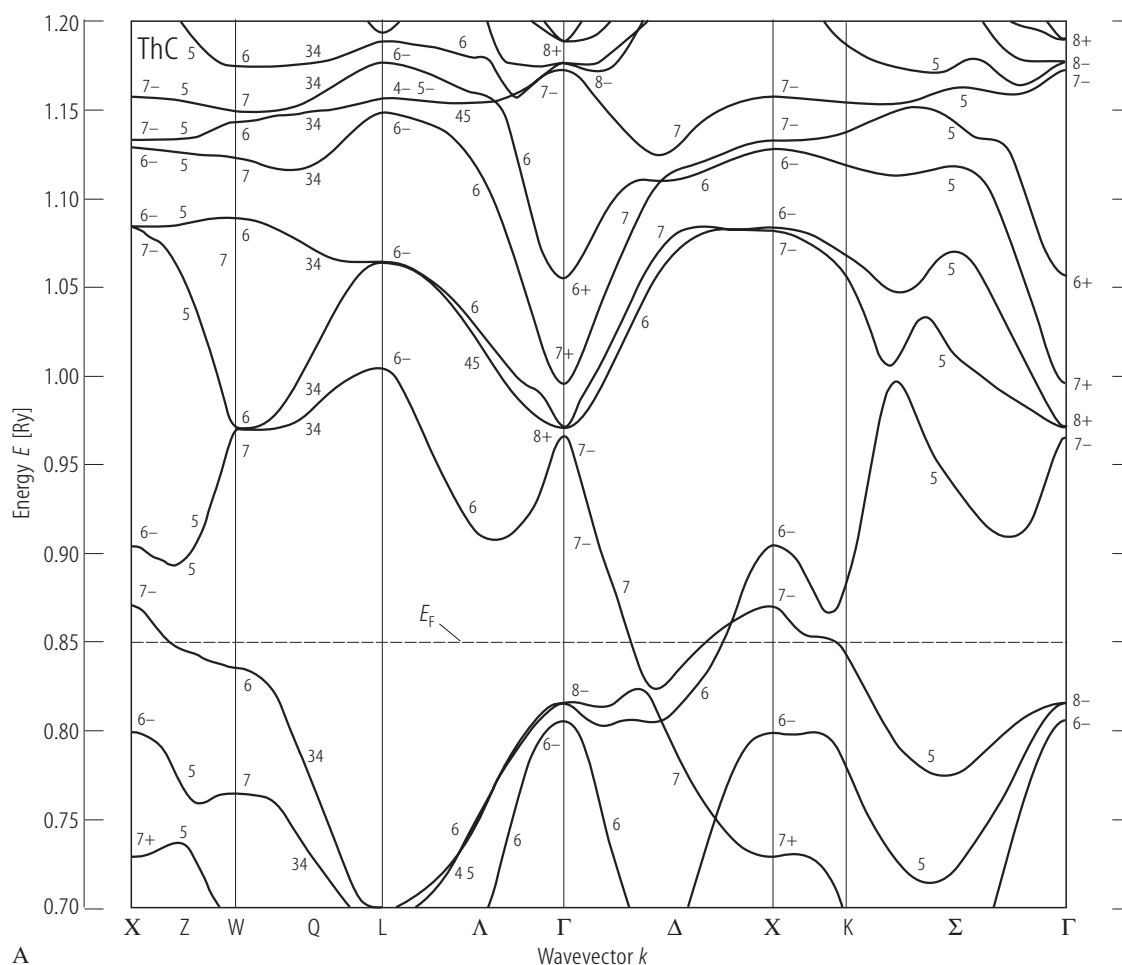


**Fig. I.8.** ThC. **(A)** Energy band structure calculated by self-consistent RAPW method [90HY1]. Note that the Fermi energy crosses the Th d band along the  $\Delta$  axis and the C p band in the vicinity of the X point. **(B)** Fermi surface: **(a)** hole sheets, **(b)** closed hole sheets, obtained by displacement of the reciprocal lattice vectors at the X point, **(c)** electron sheets [90HY1]. The hole sheet consists of three small pockets in the C 2p valence band (VB) around the X

point and the electron sheet consists of six small pockets located around the  $\Delta$  axes. There are 0.062 holes per cell and compensating number of electrons causing ThC to be a semimetal. The total DOS is 15 states/Ry cell which corresponds to  $\chi(0) = 2.6$  mJ/mol K<sup>2</sup> compared to the experimental values of 2.12 [75D2] and 2.90 mJ/mol K<sup>2</sup> [64HMM].

For Fig. I.8 (B) see next page

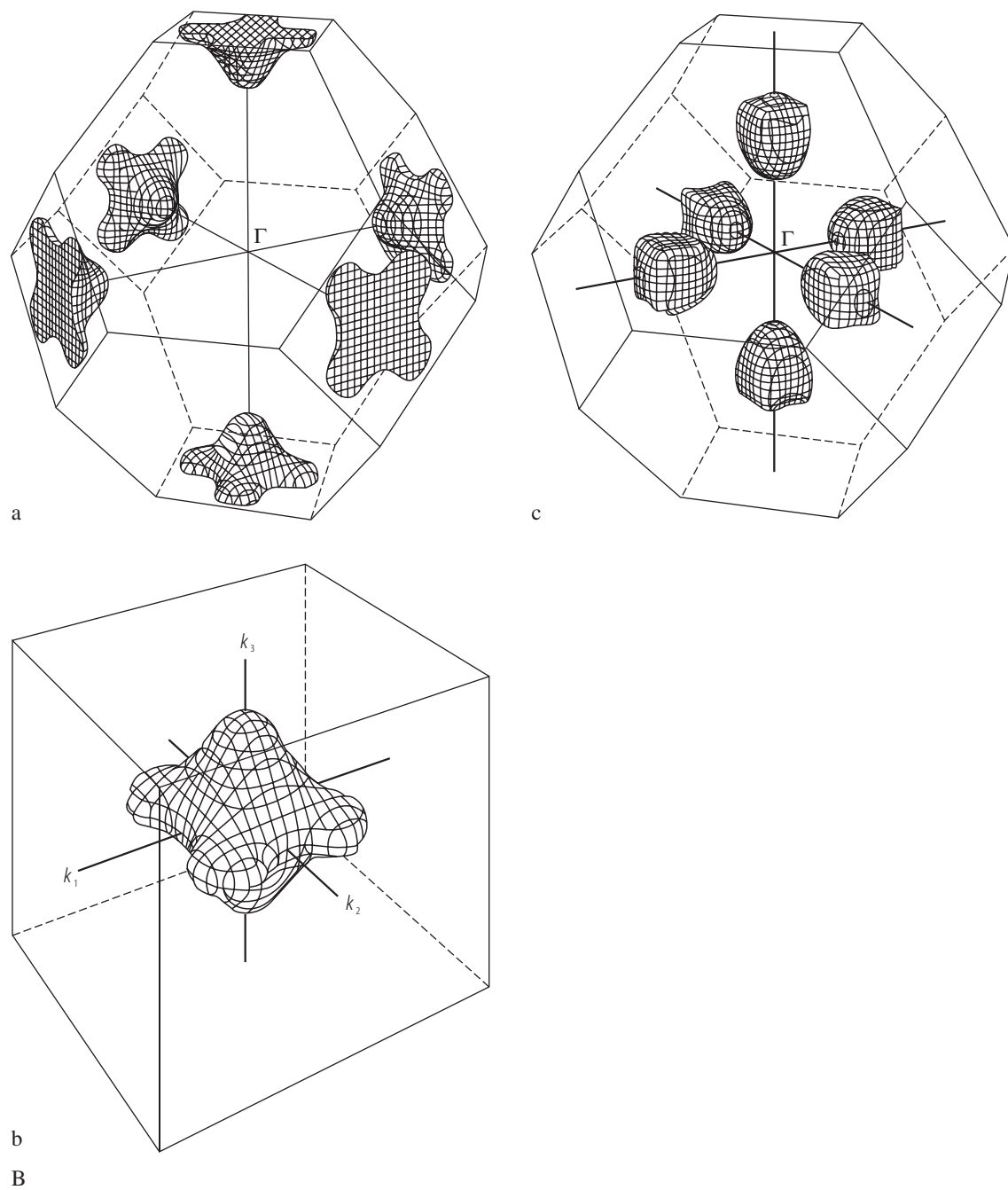


**Fig. I.8 (B).** For caption see previous page

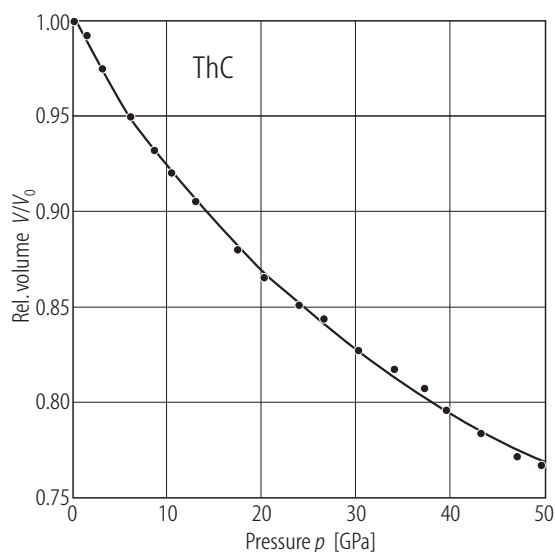


**Fig. I.9.** ThC. Relative volume  $V/V_0$  vs. pressure  $p$  up to 50 GPa [90GSBL]. Solid line is a fit to Birch and Murnaghan equations.  $B_0 = 109(4)$  GPa and  $B'_0 = 40(3)$  (see also LB III/19f2, Fig. 375).

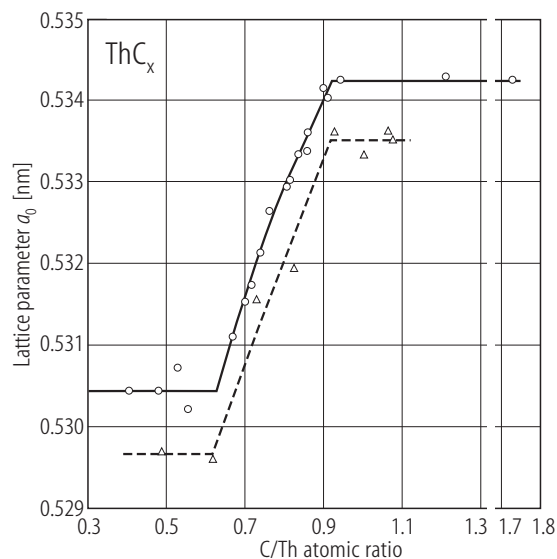


**Fig. I.10.**  $\text{ThC}_x$ . Lattice parameter,  $a_0$ , vs. the C/Th atomic ratio,  $x$ , for nonstoichiometric thorium monocarbide (open circles) [65AS]. The monocarbide phase was found to be stable from a composition of  $\text{ThC}_{0.66}$  to  $\text{ThC}_{0.96}$ . This stability range agreed with that reported by Street and Waters (unpublished) (open triangles). It is postulated that the strength of covalent bonds increases when some carbon is removed from the lattice.

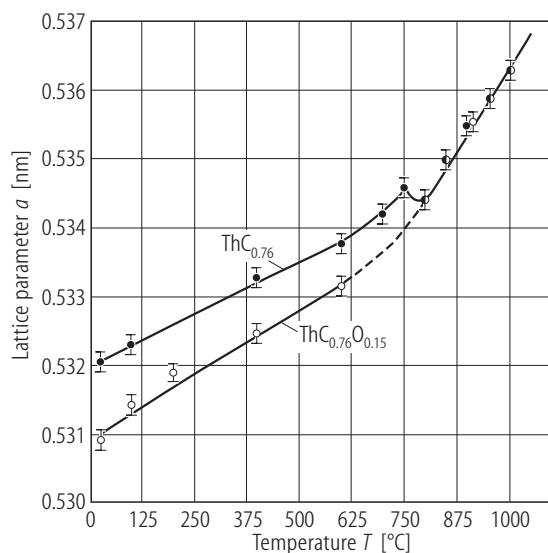


**Fig. I.11.**  $\text{ThC}_x$ . Lattice parameter,  $a$ , vs. temperature,  $T$ , for  $\text{ThC}_{0.76}$  and  $\text{ThC}_{0.76}\text{O}_{0.15}\text{N}_{0.01}$  [69LD]. Compare the transition to the superstructure at 750 °C with that at 830 °C observed for the electrical resistivity and thermal expansion [67S2] (see Fig. I.13b). For the latter carbide the X-ray refinement yields the double lattice unit cell with  $a_0 = 1.06300(8)$  nm.



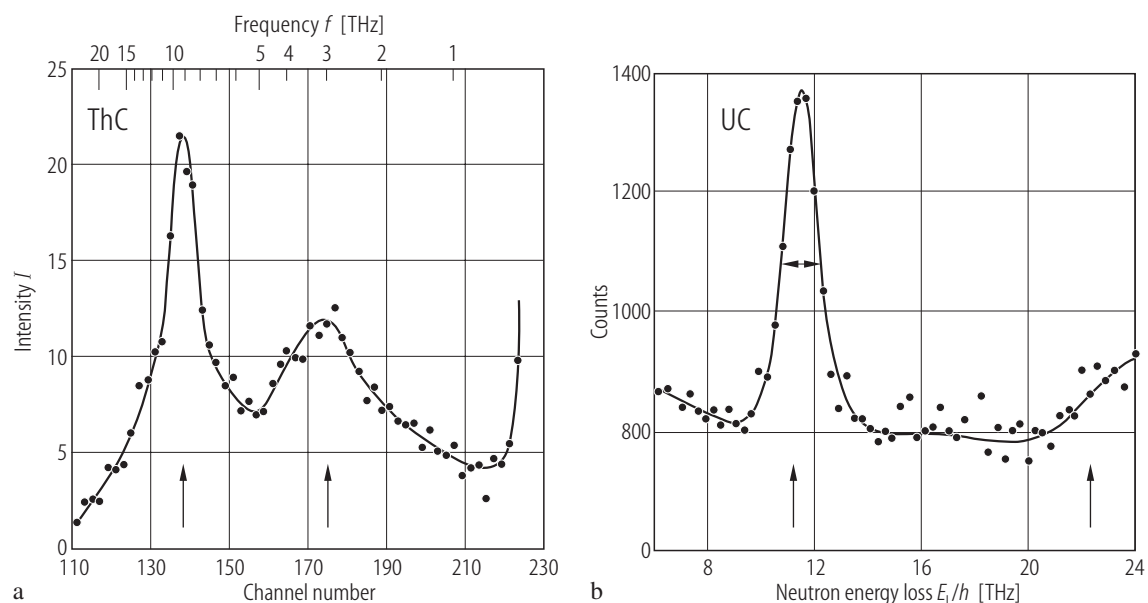


**Fig. I.12.** ThC, UC. The time-of-flight (TOF) spectra with 3 Å incident neutrons. **(a)** ThC and **(b)** UC (beryllium filter used) [74W]. The difference in phonon spectra is the lack of

separation between the optical and acoustic groups for the former, probably due to the larger size of thorium ion.

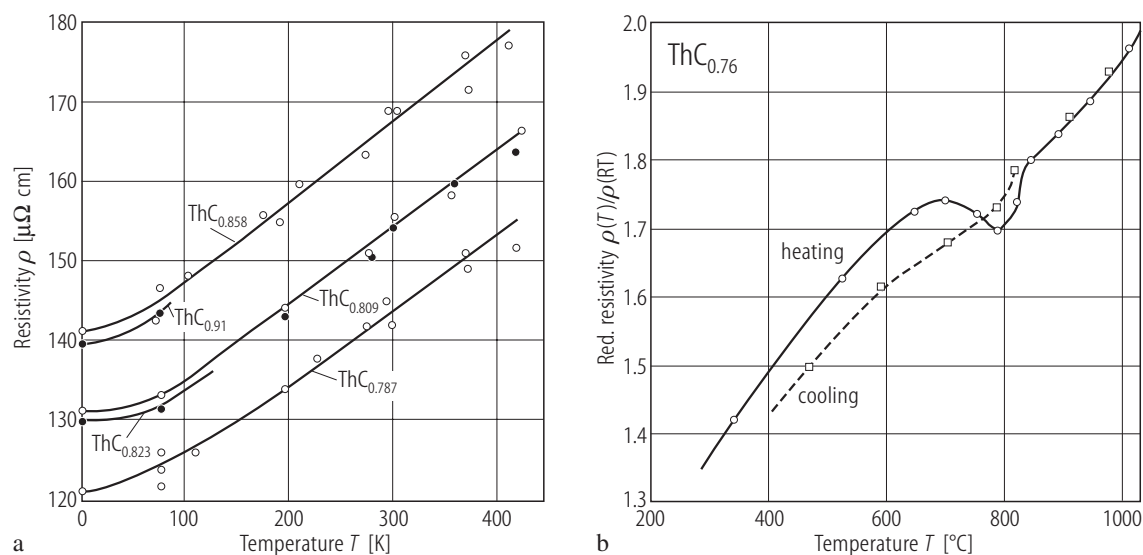


**Fig. I.13.**  $\text{ThC}_{1-x}$ . **(a)** Electrical resistivity,  $\rho$ , vs. temperature,  $T$ , for thorium carbides deficient in carbon (indicated), obtained by hot-pressing between 1250...1350 °C with a density of 90% of the theoretical one

[67AA2]. **(b)** Reduced electrical resistivity  $\rho(T)/\rho(RT)$  vs.  $T$  for  $\text{ThC}_{0.76}$  in heating and cooling cycles [67S2].  $\rho(RT) \approx 60 \mu\Omega\text{cm}$ . Compare the anomaly at 830 °C with that in the  $a_0(T)$  curve (Fig. I.11).

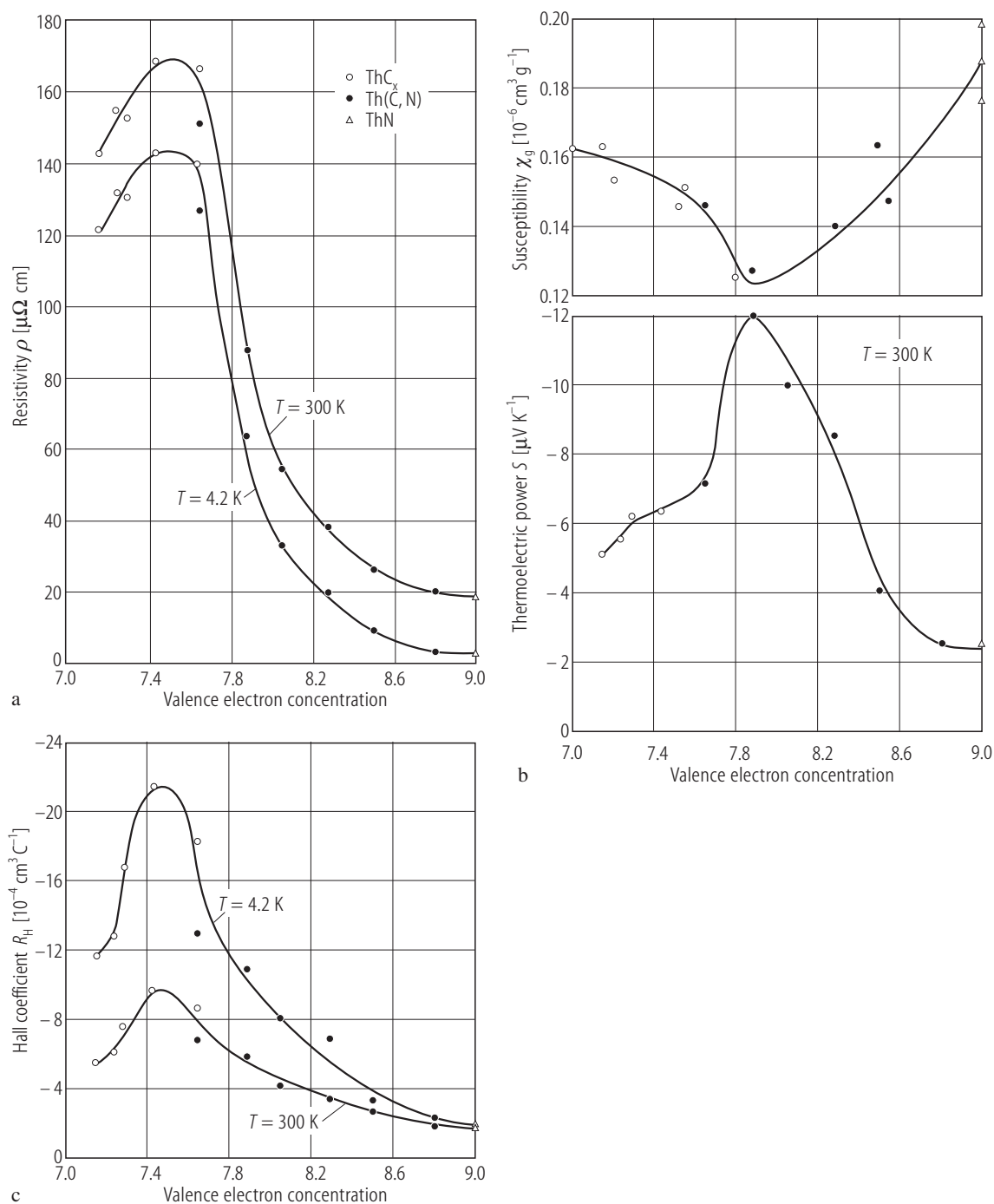


**Fig. I.14.** ThC<sub>x</sub>, ThN, Th(C,N). (a) Electrical resistivity,  $\rho$ , at 4.2 and 300 K, (b) specific susceptibility,  $\chi_g$ , [68AA] and thermoelectric power,  $S$  and (c) Hall coefficient  $R_H$  vs. valence electron concentration (VEC) for ThC<sub>x</sub> (open circles) taken from [67AA2], ThN (open triangles) taken from [67AA1] and Th(C,N) (closed circles) from [70AA]. The data proved that the same conduction mechanism is

operative for all the compositions. Hence, two overlapping bands were postulated [70AA]. Note that there is a minimum in the  $\chi_g$  vs. VEC curve at the same composition as the thermopower has its maximum. This supports an idea of the minimum in  $N(E_F)$  just at this composition, i.e. for VEC = 7.8.

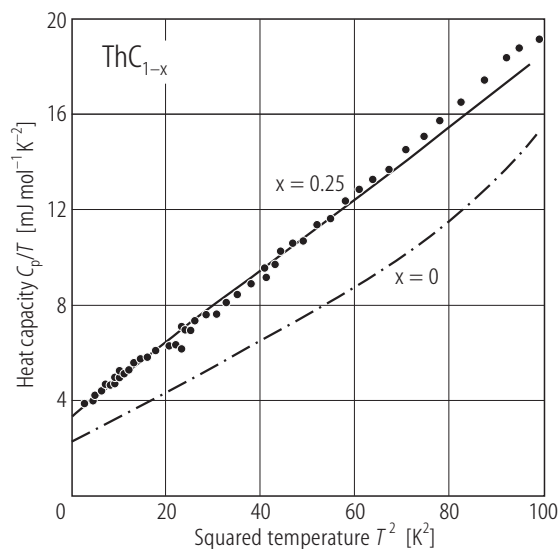


**Fig. I.15.**  $\text{ThC}_{1-x}$  ( $x = 0.25$ ). The plot  $C_p/T$  vs.  $T^2$  in the range 2...10 K (closed points) [79MBA], compared to the data of ThC ( $x = 0$ ) (dot-dashed curve) taken from [75D2].  $\chi(0) = 3.38 \text{ mJ/mol K}^2$ ,  $\Theta_D = 238 \text{ K}$ .

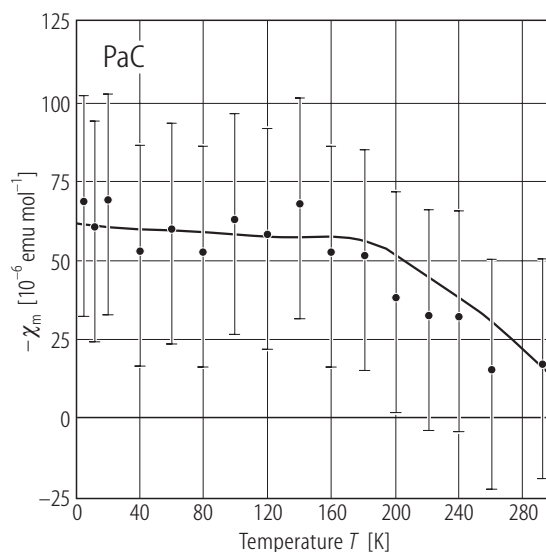


**Fig. I.16.** PaC. Molar magnetic susceptibility,  $\chi_m$ , vs. temperature,  $T$ , [77HWBD]. The weak temperature dependence of PaC indicates the absence of 5f electrons and the  $\text{Pa}^{5+}$  state in this compound.

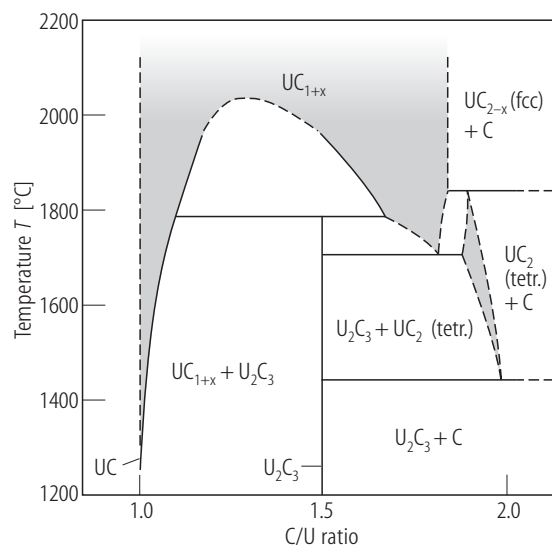


**Fig. I.17.**  $\text{UC}_{1+x}$ . The most thoroughly documented phase diagram around UC composition [70LB]. The large shaded area presents the possibility of UC to dissolve carbon at high temperatures. This can be treated as the complete solubility with cubic  $\text{UC}_2$  as it is case also for ThC and  $\text{ThC}_2$  [69BS]. Therefore, at high temperature those solid solutions form single carbon atoms and bound carbon pairs probably randomly distributed in the octahedral sites of the fcc metal sublattice (see e.g. [76D]).

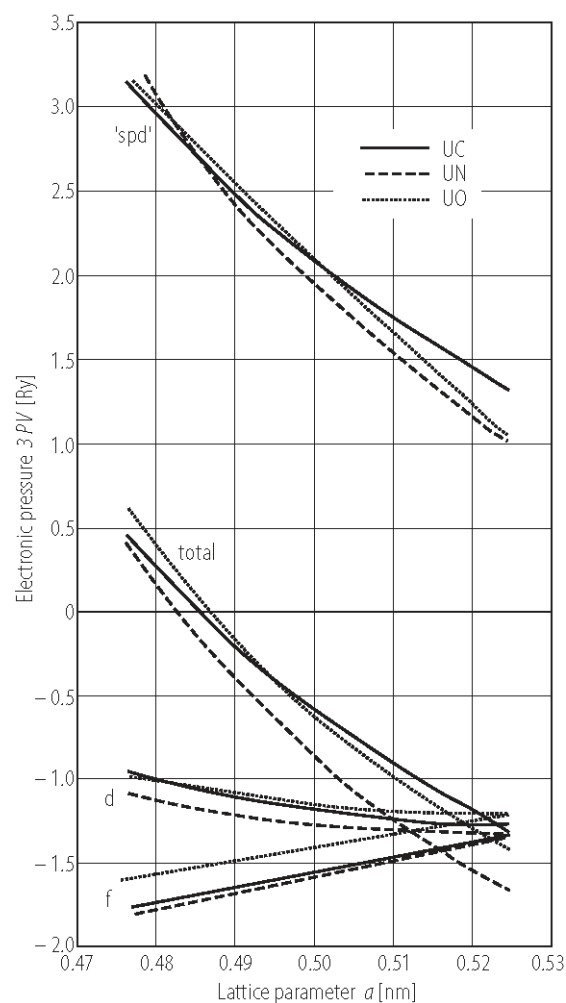


**Fig. 1.18.** UC, UN, UO. The electronic pressure,  $3PV$ , as a function of lattice parameter, at the zero temperature *equation of state* (see “total” curve) [84BJS]. See also the uranium partial f and d contributions. The curves labeled “spd” are the contributions from the remaining valence electrons plus Madelung contributions, which at equilibrium is equal to  $-0.2$  Ry ( $\equiv 3$  GPa). The theoretical equilibrium lattice parameters are directly obtained and compared with the experimental lattice parameters (see the Table below). Note that the magnitude of the f-partial contribution to the total pressure is large of about  $-1.6$  Ry ( $\equiv 40$  GPa) and comparable to that in metallic uranium. This indicates the large f contributions to chemical bonding. The bulk moduli were also calculated and presented in the Table below:

	UC	UN	UO
Lattice parameters $a$ [nm]			
Theory	0.485	0.483	0.488
Experiment	0.495	0.489	0.492
Bulk modulus $B_0$ [GPa]			
Theory	168	241	198
Experiment	159	193	—

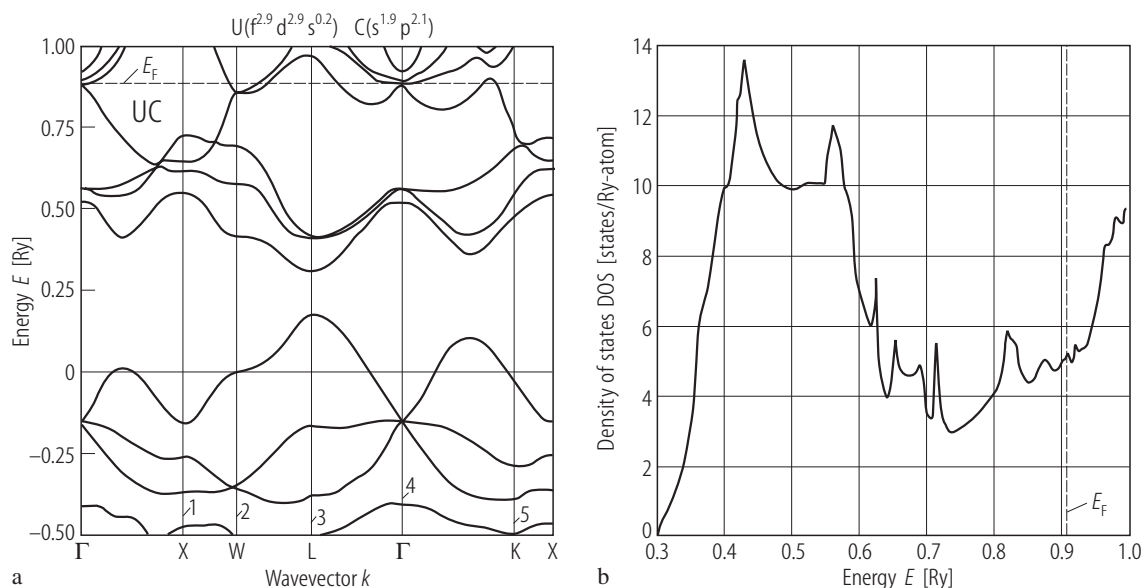


**Fig. 1.19.** UC. **(a)** The RAPW energy band structure with an exchange parameter,  $\alpha = 2/3$  [77FK]. Three bands at the bottom are the strongly mixed U 6d – C 2p bands with only 1 % admixture of U 5f character. The bands above the gap.

are f-p bands. At the top there are d-bands lying close to f-band situated around  $E_F$ . **(b)** DOS. An enhancement factor in  $\gamma(0)$  is nearly equal to 10 [77FK].

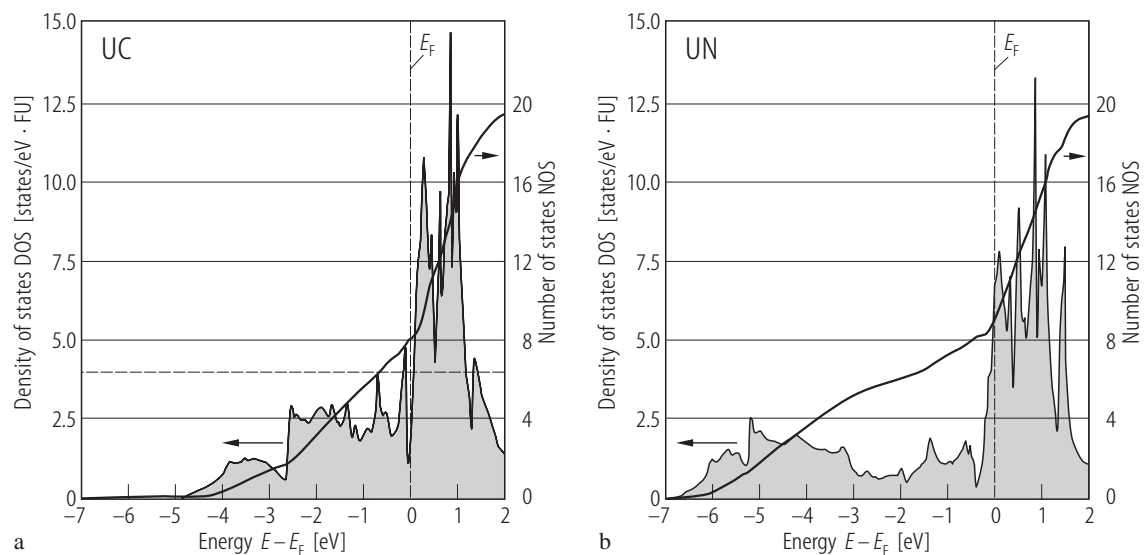


**Fig. 1.20.** UC, UN. Total DOS (lhs) and NOS (rhs) functions for **(a)** UC and **(b)** UN calculated by the combination of self-consistent energy band and DFT [85B2] taking the effective Stoner parameter of 0.5 eV for these compounds. The Stoner criterion for the onset of

ferromagnetism is satisfied for UN but not satisfied for UC, due to a small DOS at  $E_F$ , being lower than the required value of 4 states/eV F.U. (see the Figure). For partial f and p DOS and NOS see Ref. [84B1, 3].

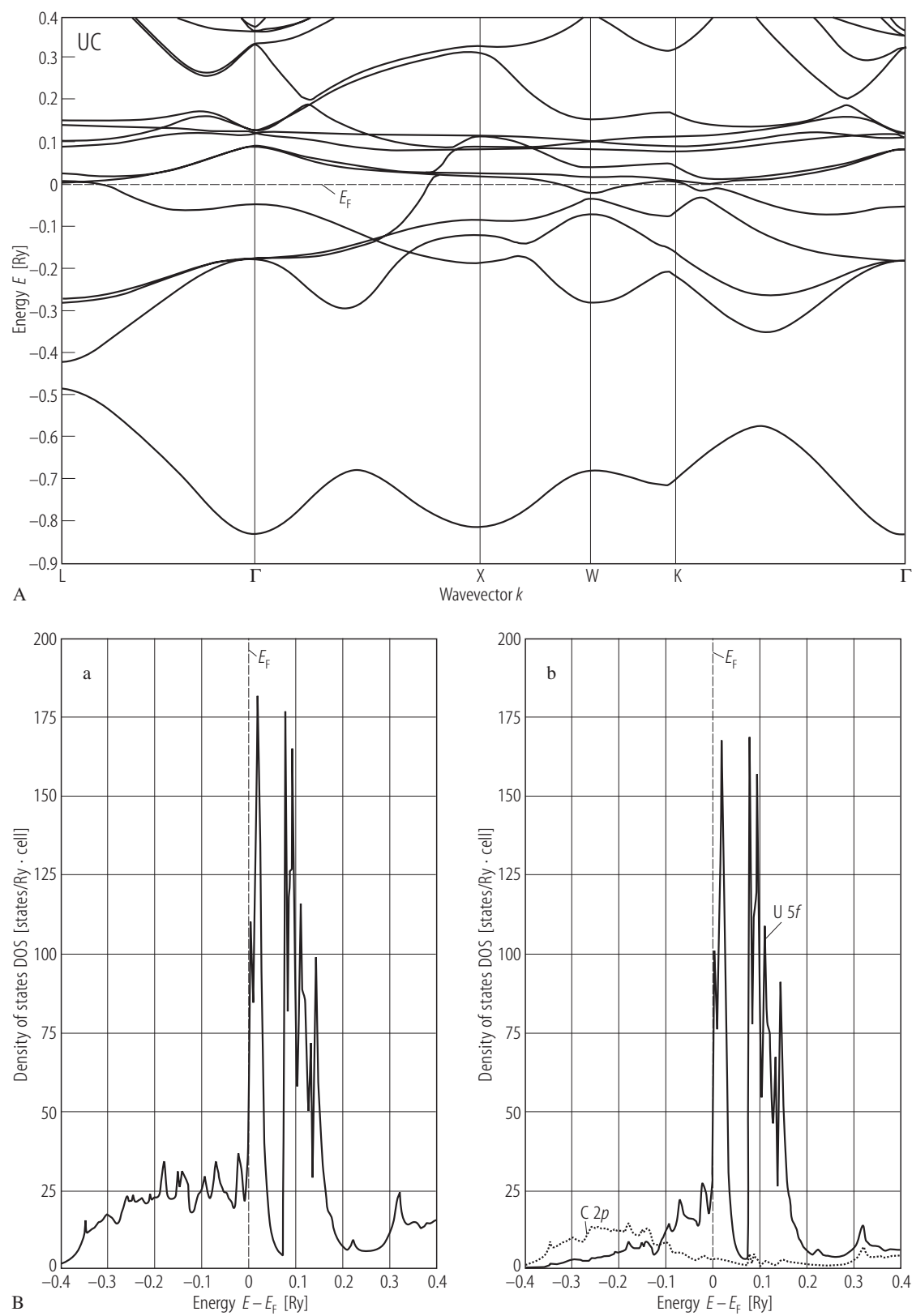


**Fig. I.21 (A), (B).** For caption see next page.

UC

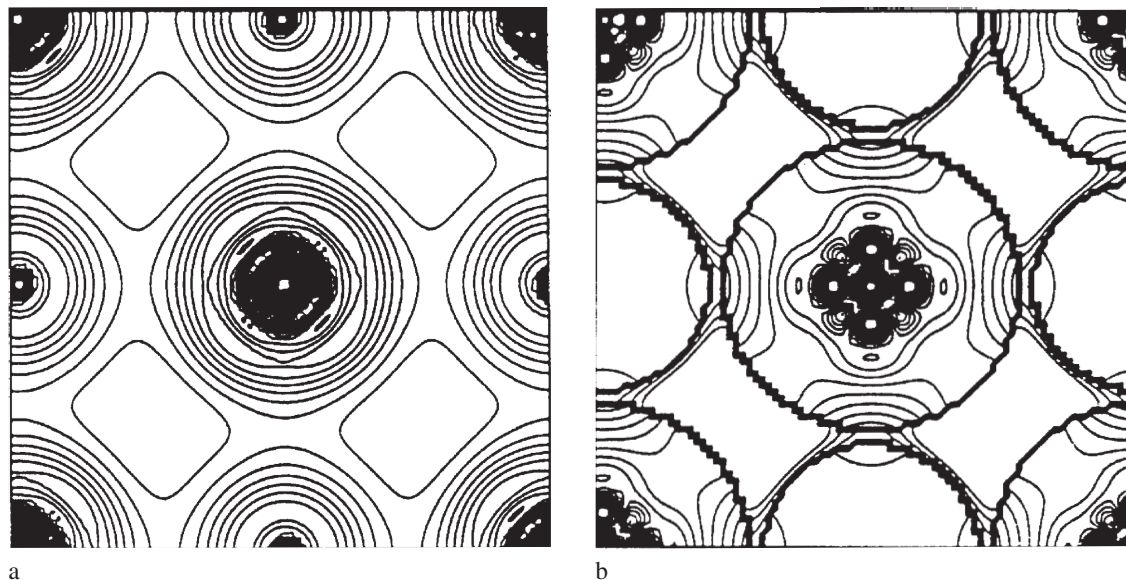


**Fig. 1.21.** UC. **(A)** Energy bands calculated by fully relativistic LMTO with including spin orbit coupling (SOC) and within the framework of LSDA [95TWB].  $E_F$  is marked by the horizontal dashed line. Compare these results with those reported in [99YHIM] and those presented in Fig. 1.20. **(B)** **(a)** DOS and **(b)** partial DOS of U 5f (solid line) and C 2p (dashed line) derived from the RLMT0 + spin orbital inclusion in LSDA [95TWB].  $E_F$  is at zero energy and is marked with the vertical line. Due to the spin orbit interaction the 5f band is split by about 0.1 Ry into a  $5f_{5/2}$  and a  $5f_{7/2}$  partial DOS. The C 2p DOS is centered at  $\sim 0.2$  Ry below  $E_F$  and overlaps with the U 5f states, which leads to a substantial p-f hybridization. The value of DOS at  $E_F$  is

50 states/Ry and is higher than the values reported in other calculations, such as in [84B1] and [99YHIM]. The Stoner product  $IN(E_F) = 0.9$ . **(C)** Calculated **(a)** full charge density contour and **(b)** monospherical charge density component, both on (001) plane (see the text [95TWB]). The uranium atoms are located at the corners of the figure and one of them in the middle. The C atoms are located on the axis connecting the U atoms. Note that the charge density of the C atoms is spherical, whereas that of the U atoms has a large degree of directionality, showing lobes pointing in the direction to the nearest carbon atom (covalent contribution accompanying the metallic binding).

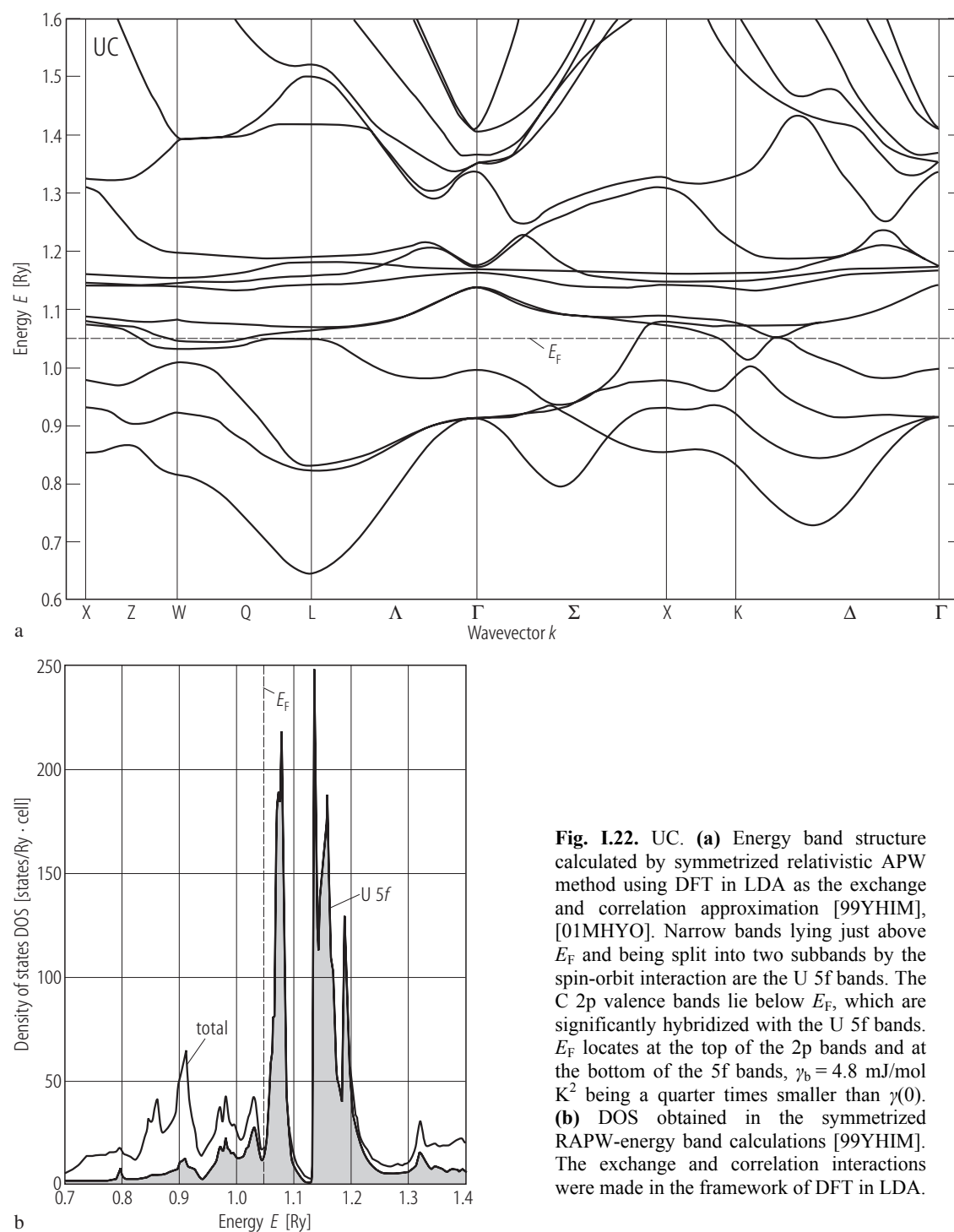


**Fig. 1.22.** UC. (a) Energy band structure calculated by symmetrized relativistic APW method using DFT in LDA as the exchange and correlation approximation [99YHIM], [01MHYO]. Narrow bands lying just above  $E_F$  and being split into two subbands by the spin-orbit interaction are the U 5f bands. The C 2p valence bands lie below  $E_F$ , which are significantly hybridized with the U 5f bands.  $E_F$  locates at the top of the 2p bands and at the bottom of the 5f bands,  $\gamma_b = 4.8$  mJ/mol  $K^2$  being a quarter times smaller than  $\gamma(0)$ . (b) DOS obtained in the symmetrized RAPW-energy band calculations [99YHIM]. The exchange and correlation interactions were made in the framework of DFT in LDA.



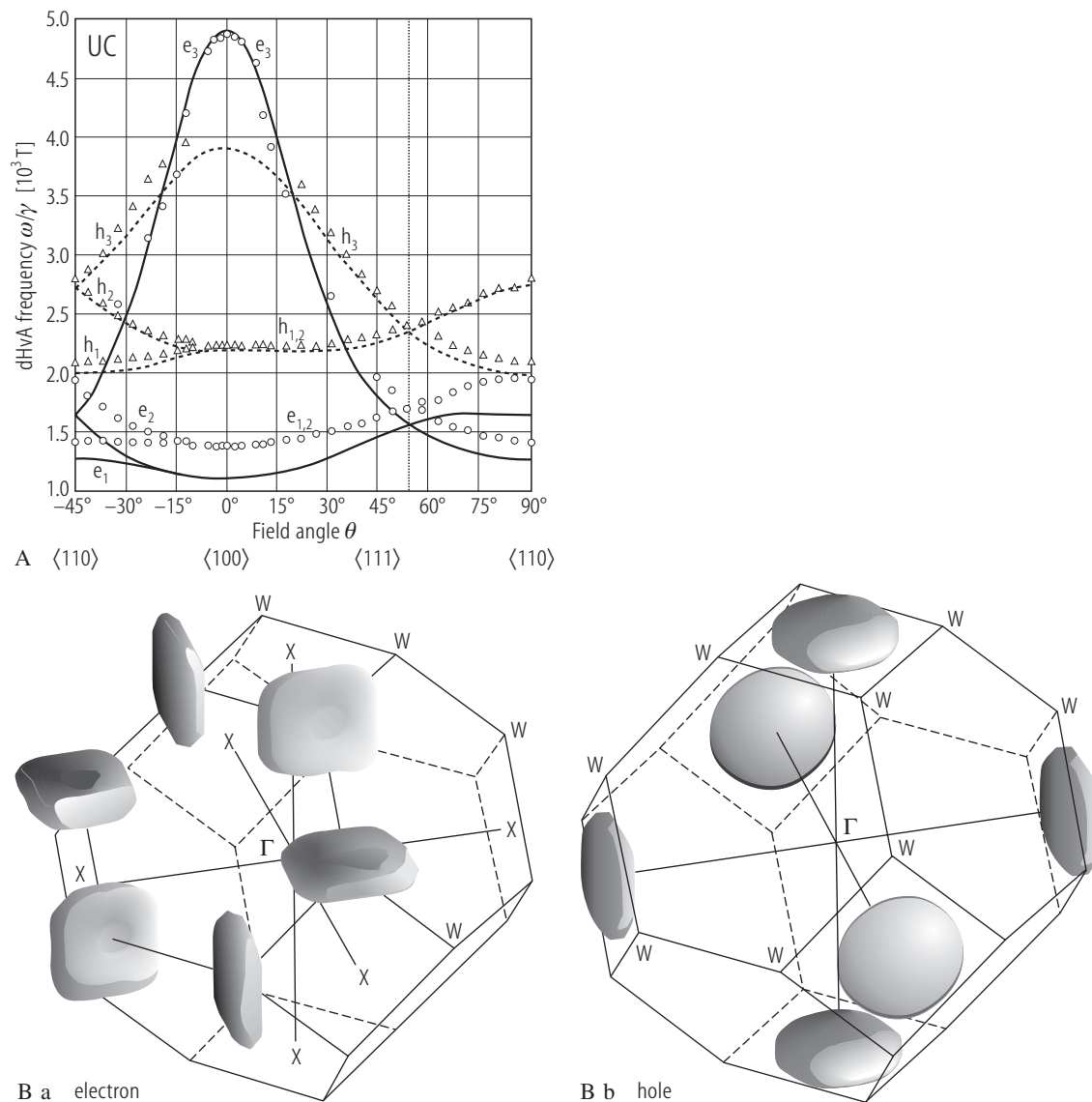


**Fig. 1.23.** UC s.c. **(A)** Angular dependence of the dHvA frequency (experimental points) of the UC sample (RRR = 230) measured at 30 mK and 17 T, compared to the results of band calculations (solid and broken lines) [99YHIM]. Note three kinds of dHvA branches denoted as  $e_{1,2}$ ,  $e_3$  and  $h_{1,2}$ , their second harmonics and a sum-frequency  $e_{1,2} + h_{1,2}$  with the cyclotron mass  $m_c$  being equal to  $4.7 m_0$  for the branches  $e_{1,2}$ ,  $15 m_0$  for  $e_3$  and  $1.5 m_0$  for  $h_{1,2}$  one. The mass enhancement is larger for the electron Fermi surface due to originating from the U 5f electrons. The mass enhancements didn't allow to observe dHvA signals around

(100) in earlier report (see Ref. [90OUKS] and Fig. 384 in LBIII/19f2) due to a worse quality of the UC sample. The experimental cyclotron masses of holes are about twice as large as the calculated ones. In the case of the  $e_3$  branch even four times [01MHYO]. **(B)** The Fermi surfaces are: **(a)** centered at the W points, consisting of six cushion-like electron sheets, originating from the U 5f conduction band and **(b)** centered at the X points consisting of three ellipsoidal hole sheets originating from the C 2p valence band. The carrier numbers of electrons and holes are equal as expected for a semimetal [99YHIM].

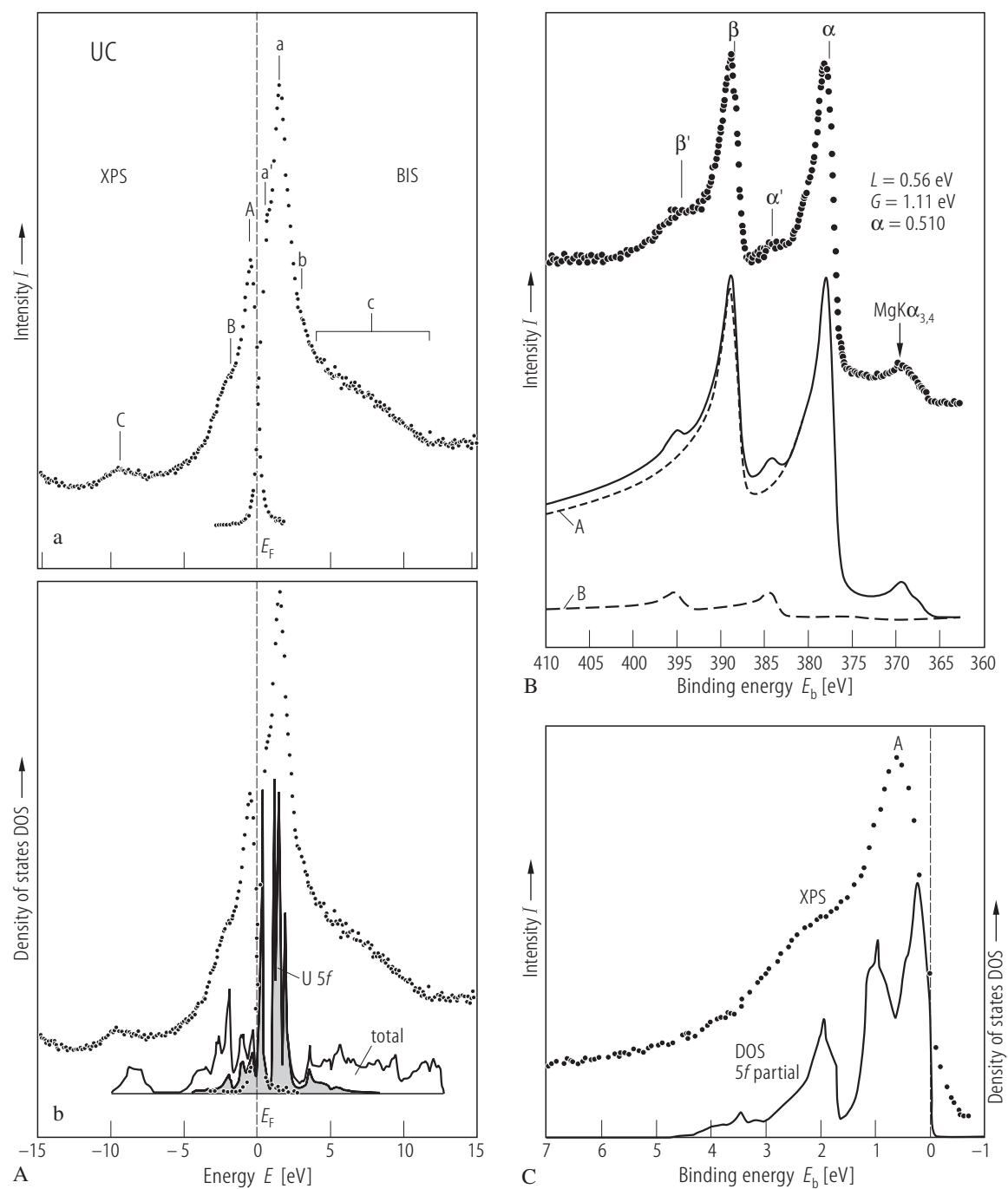


**Fig. I.24.** For caption see next page.

**Fig. I.24.** UC s.c. **(A)** (a) XPS and BIS spectra connected together at the Fermi edge to get there the equal intensities [93EMST]. The sharp peaks A, a and a' and the long tailing c are ascribed to the U 5f states. The shoulders B and b originate predominantly from the U 5f states with some overlap with the U 6d states. The hump C is the C 2s band. **(b)** DOS calculated using a self-consistent relativistic APW method [90HY1]. Note that the one-electron picture of DOS explains only a part of the observed valence state EDC, which does not show a predicted composite structure above  $E_F$  [93I]. **(B)** The U 4f core level spectrum (upper curve) and the results of the Doniach-Šunjić line shape analysis based on the singularity index  $\alpha$  (lower curve) [93EMST].  $\alpha$  and  $\beta$  are spin-orbit-split pairs corresponding to  $4f_{7/2}$  and  $4f_{5/2}$  with satellites  $\alpha'$  and  $\beta'$ , respectively. The presence of the satellites  $\alpha'$  and  $\beta'$  indicates the more-localized nature of the U 5f states in UC. They can be interpreted in terms of the impurity Anderson model (see for example Ref. [88GSHS]). Solid line and broken lines A and B are convoluted and deconvoluted curves respectively. The parameter  $L$  is the Lorentzian width while that of  $G$  is the Gaussian width. **(C)** Experimental XPS valence state EDC [93I] compared to the theoretically calculated curve of the 5f partial-DOS [90HY1]. Note that the main peak A of the experimental curve does not show a composite structure. In the calculated total DOS curve, a sharp and intense peak exists below  $E_F$  (not shown) with disagreement with the experiment.

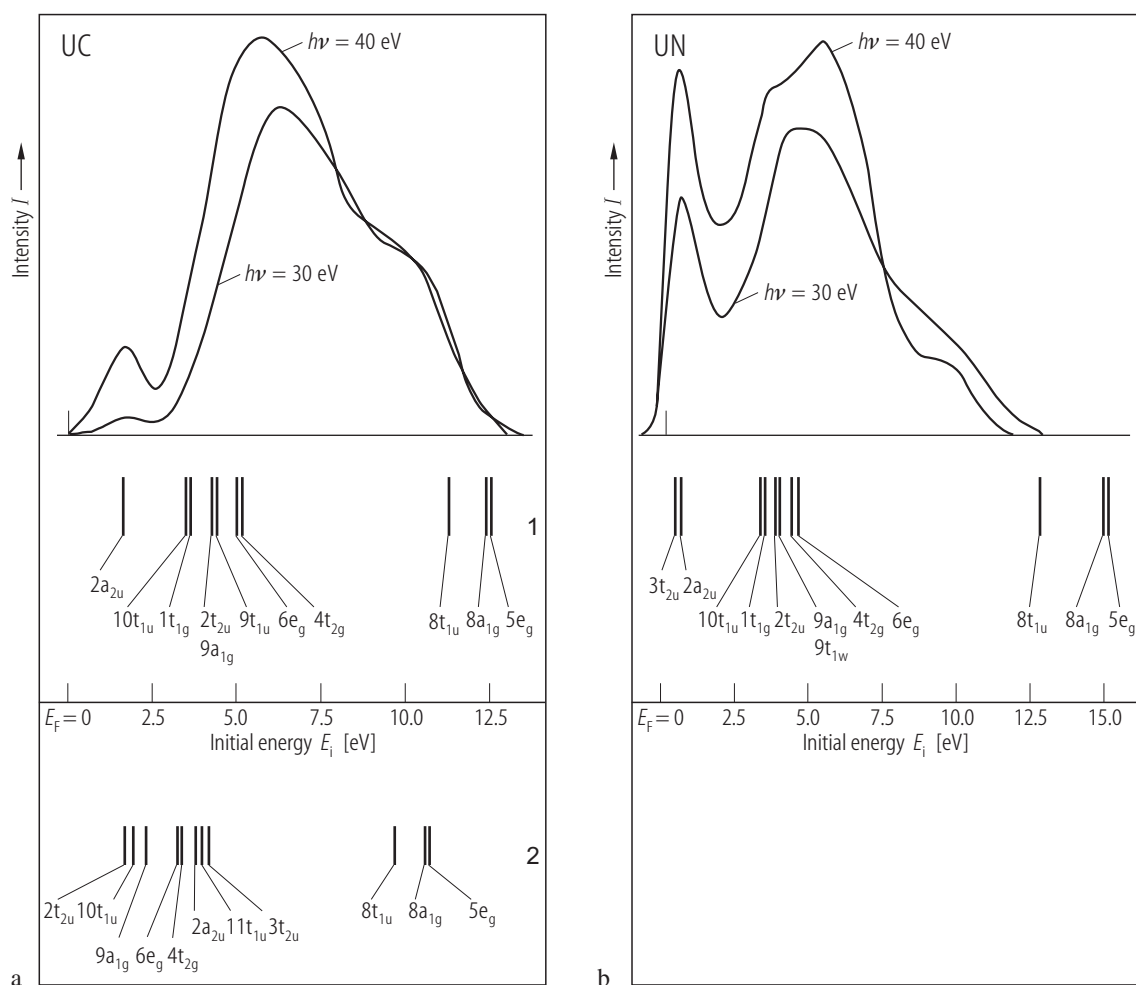


**Fig. I.25.** UC, UN. Self-consistent molecular orbital (MO) calculations of electronic structure of **(a)** UC and **(b)** UN [80JG] (for details see also [80ZGW]). The calculations were performed for octahedrons  $UC_6^{20-}$  and  $UN_6^{15-}$  by the spin-restricted  $X_\alpha$  discrete variational method (DVM). The calculated energy levels and experimental EDC's taken at two different photon energies from [79EK2] are given at the bottom and top of the figures respectively. The upper set of

energy levels of UC is obtained in self-consistent while the lower one in non-consistent processes. For UN only the latter diagram is shown. The series of MO's  $2a_{2u}$ ,  $3t_{2u}$  is composed fully of 5f atomic orbitals (AO) while that of  $10t_u$  has an admixture of AO 2pC(N). Note for UN the existence of an additional electron on  $3t_{2u}$  compared to UC which corresponds to the increase of the intensity of the first band in EDC, when going from UC to UN.

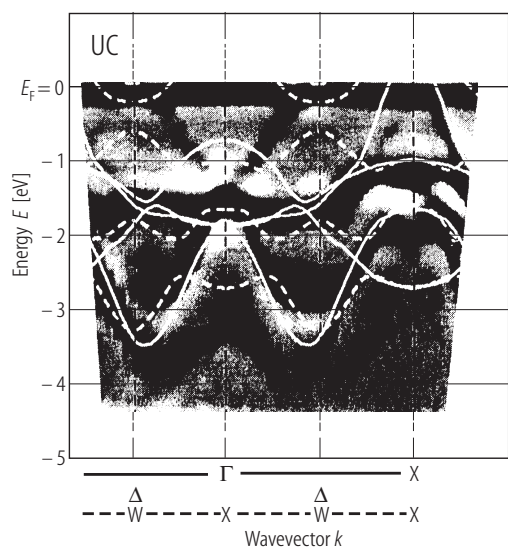


**Fig. I.26.** UC s.c. Experimental band structure derived from high-resolution ARPES measurements [01IKTY]. The energy bands (dark areas) are compared to band structure calculations along  $\Gamma X$  (white solid lines) and  $XWX$  (white dashed lines) high symmetry lines taken from [99YHIM]. According to the band calculations the VB consists mainly of C 2p states while bands near  $E_F$  have a strong U 5f-C 2p or U 5f-U 6d hybridized character. Only near  $E_F$  there are some differences between the experimental and theoretical data. For example, no electron pocket at  $\Gamma(X)$  point exists as predicted by the band calculations. (For detailed description see the original paper).

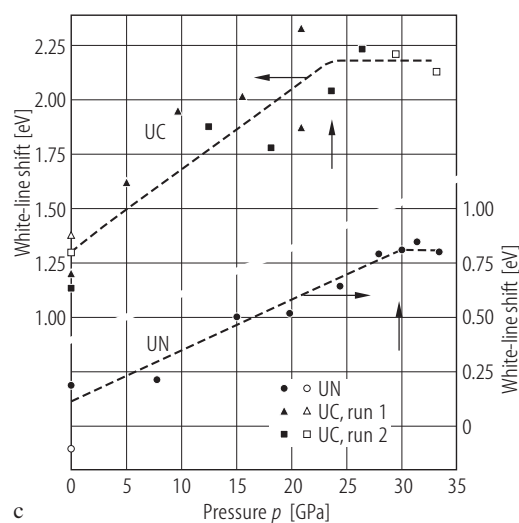
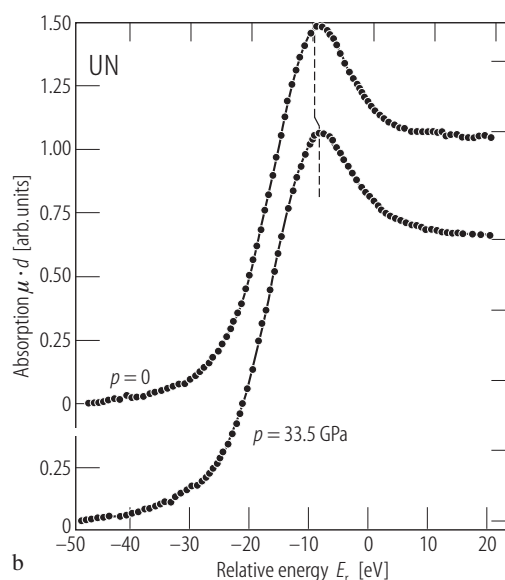
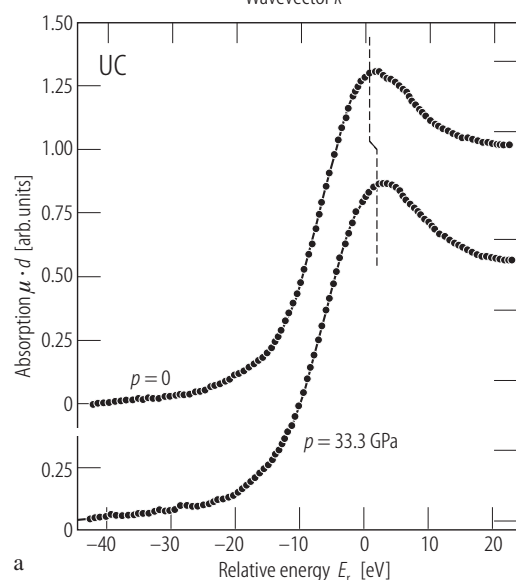


**Fig. I.27.** UC, UN. X-ray absorption near-edge structure at the U- $L_3$  threshold (XANES) for: **(a)** UC and **(b)** UN for ambient pressure  $p$  and 33.3 GPa [90BKSV]. **(c)** Pressure dependence of the white-lines (WL) shift relative to  $UF_4$  [90BKSV]. Note that for both those compounds the WL-lines shift to higher energies with increasing pressure due to increasing 5f-delocalization, which is attributed to decreasing of the 5f occupancy. The vertical arrows indicate changes in slope, which occur at pressures of 27 and 29 GPa, respectively, where structural phase transitions take place (see Figs. I.29 and II.31).

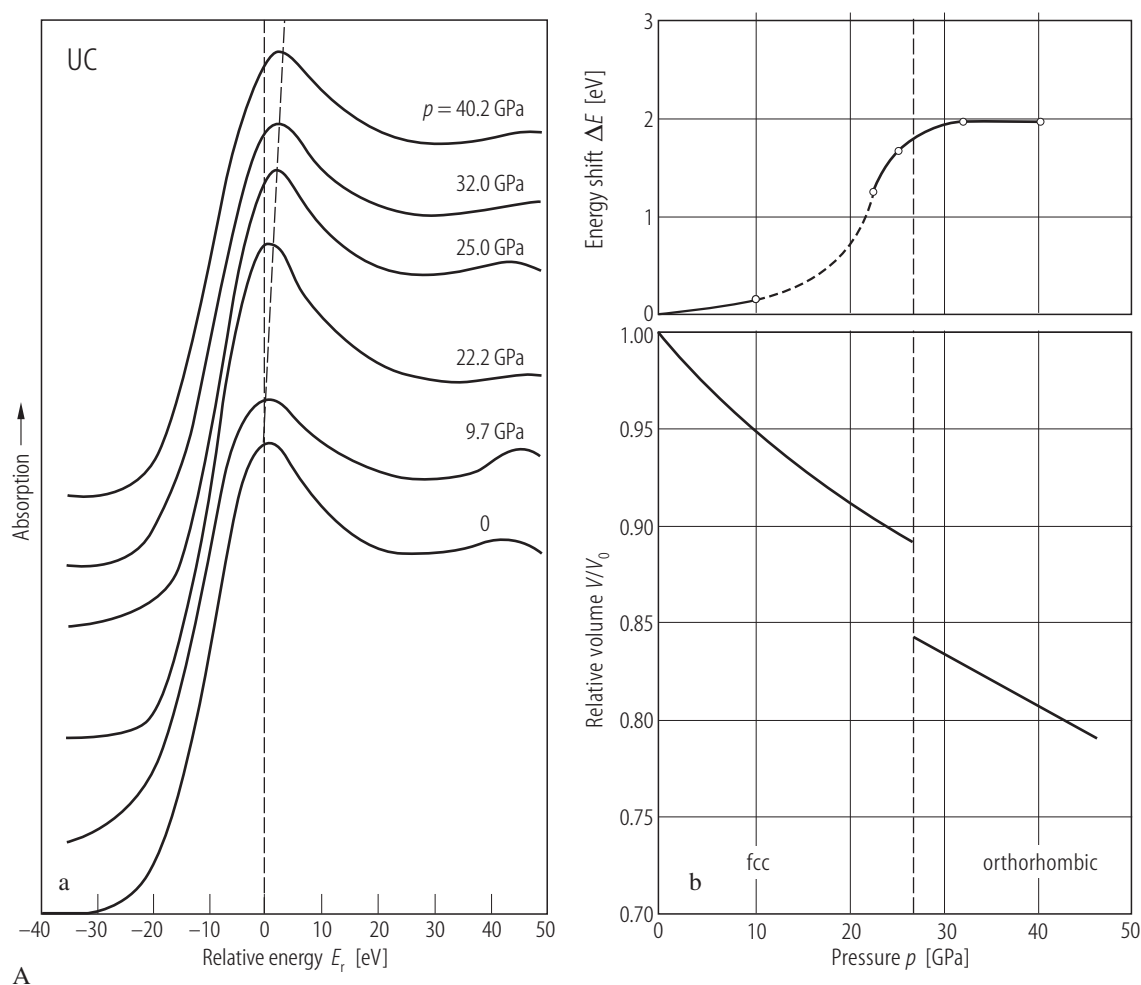


**Fig. I.28.** UC. **(A)** **(a)** XANES spectra at the U- $L_3$  threshold [87IBDD]. **(b)** Energy shift,  $\Delta E$ , under pressure at the maximum  $L_3$  absorption edge of uranium (upper curve) with the unit cell volume change (lower curve) [87IBDD]. The nature of the shift of the  $L_3$ -edge to higher energy and the occurrence of the phase transition at 27 GPa [86SGBI] indicate the increasing 5f-delocalization and following

decreasing 5f occupancy. **(B)** **(a)** Near-edge structure taken at 8 GPa and 42 GPa, showing a white line above the  $L_3$ -edge, corresponding to the transition to the 6d states [86SGBI]. **(b)** Position of the white line as a function of pressure up to 42 GPa [86SGBI]. Note no change in this position with pressure, which indicates a constant value in transition energy.

For Fig. I.28 (B) see next page

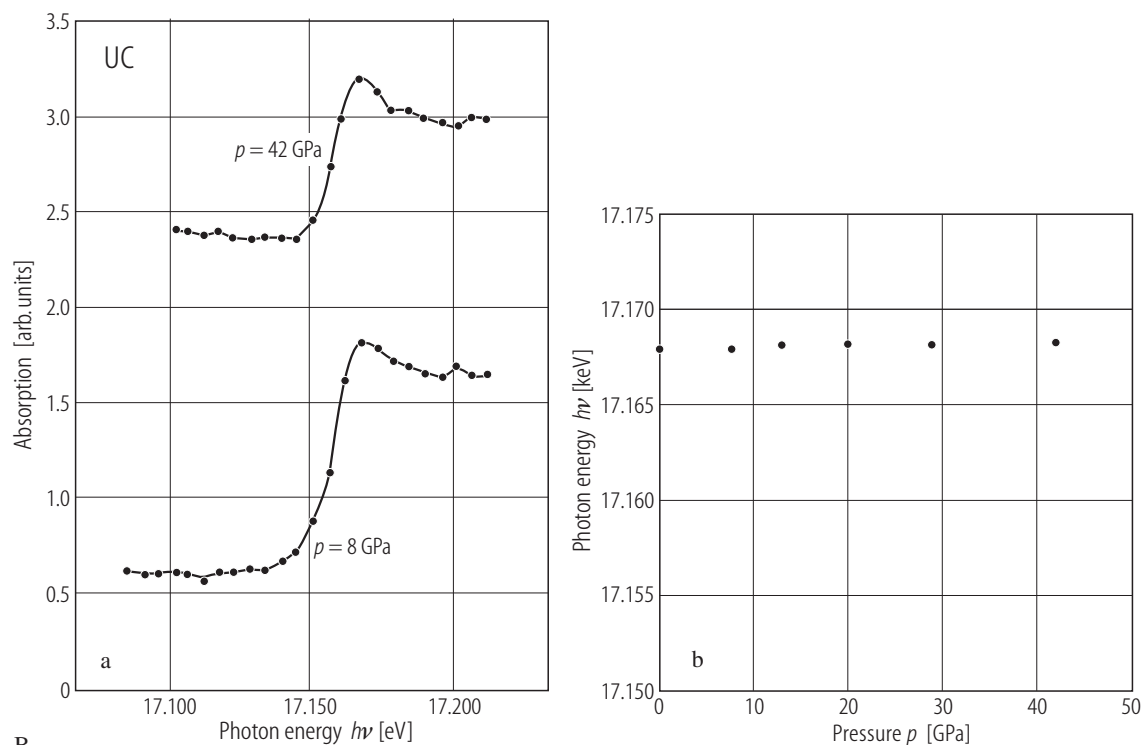


**Fig. 1.28(B).** For caption see previous page.

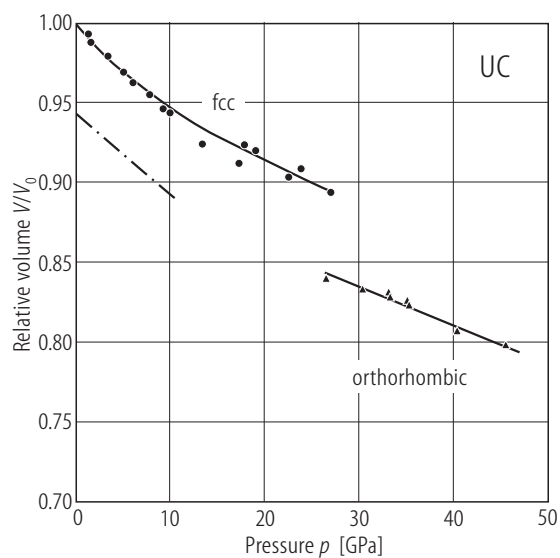


**Fig. 1.29.** UC. Relative volume,  $V/V_0$ , vs. pressure,  $p$ , up to 50 GPa [86SGBI]. No hysteresis was observed.  $a_0 = 0.49606(5)$  nm. The solid line for the cubic phase is stable for  $p < 27$  GPa and calculated from the Murnaghan equation using  $B_0 = 155$  GPa and  $B_0' = 7.9$ . These values found from the limited range  $p < 11$  GPa are 160(4) and 3.6(5), respectively. The dot-dashed line describes a theoretical equation of state [83B1].  $B_0^{\text{th}} = 168$ ,  $a_0^{\text{th}} = 0.485$  nm. The high pressure-phase ( $p > 27$  GPa) is a distortion of the body-centered tetragonal unit cell of the fcc lattice. The transformation in UC (27 GPa) happens at a similar value found in UN (29 GPa), where for both compounds the U-U distance has decreased to about 0.334...0.338 nm. See also Fig. 378 in LBIII/19f2.

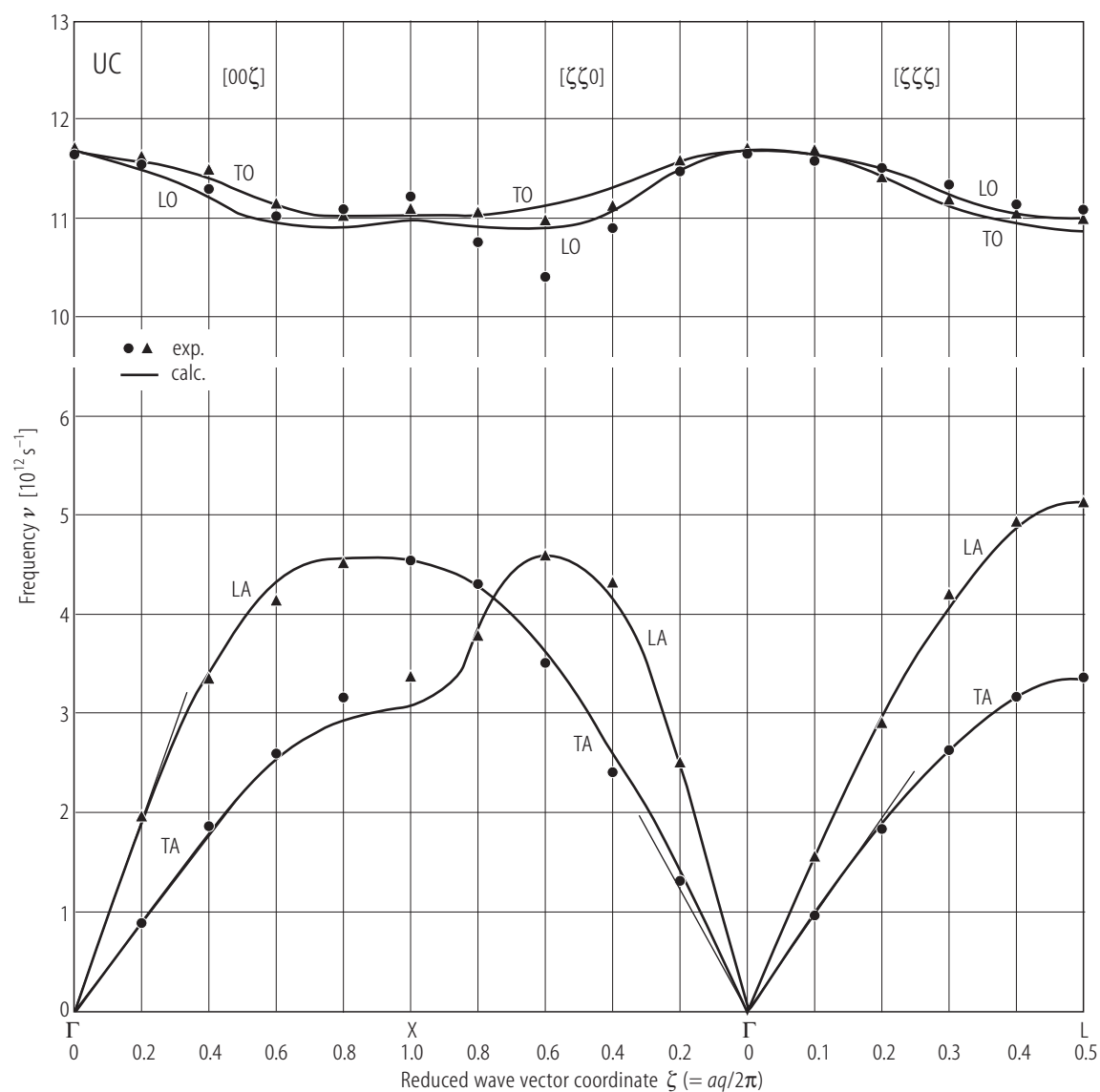


**Fig. I.30.** UC. Phonon dispersion curves (PDC) [71SG]. The dispersion relation is fitted by a second-neighbour Born-von Kármán short-range force constant analysis. The acoustic modes (A) occur below 5 THz while the optic

modes (O) are grouped between 10.3...11.7 THz frequencies. T and L mean transverse and longitudinal modes, respectively. (Also presented in LBIII/19f2, Fig. 379).

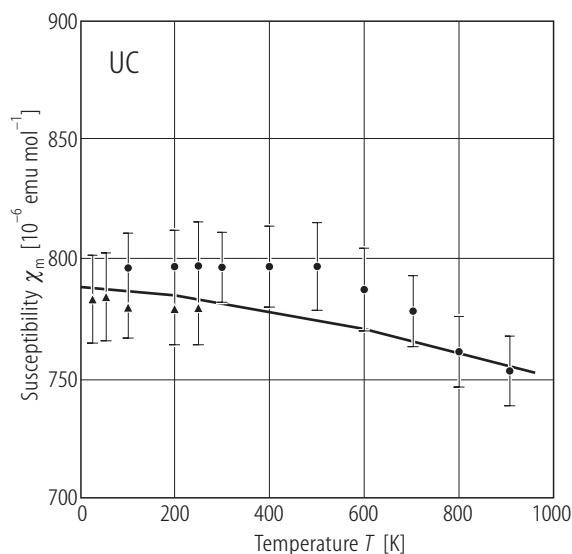


**Fig. I.31.** UC. Molar magnetic susceptibility,  $\chi_m$ , vs. temperature,  $T$ , up to 900 K taken from [74CL]. Experimental points: solid triangles are data from [67LNRM] and closed circles from [64BU]. The solid line is calculated based on  $5f^2$  configuration. The calculation in IC scheme is based on a truncated basis set taking into account 8-free-ion  $J$  manifolds and crystal field parameters  $A_4\langle r^4 \rangle = 2365 \text{ cm}^{-1}$  and  $A_6\langle r^6 \rangle = 156 \text{ cm}^{-1}$ . This leads to the first excited states at  $2267 \text{ cm}^{-1}$  [74CL]. See also LBIII/19f2, Fig. 381, for  $\chi_m$  results of different authors.

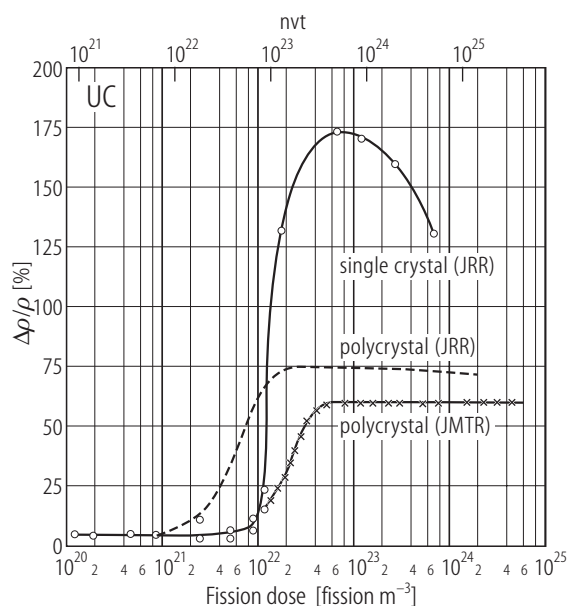


**Fig. I.33.** UC s.c. Induced electrical resistivity increment ratio  $\Delta\rho/\rho$  vs. fission dose (units  $\text{f/m}^3$ ) for a single crystal (open circles) and polycrystalline samples [81MHK] (dashed and solid curves) irradiated in two different test reactors (marked) [90MTHK]. Note that especially for the single-crystalline sample a large change in the electrical resistivity at about  $10^{22} \text{ f/m}^3$  fission dose occurs.

For Fig. I.32 see next page

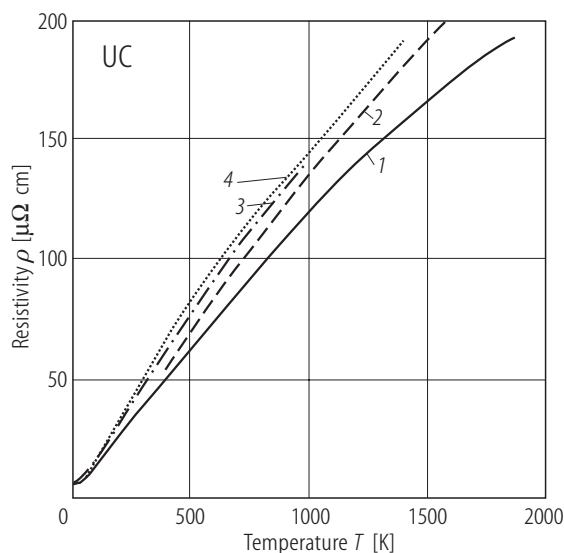


**Fig. I.34.** UC. High-temperature electrical resistivity  $\rho$  vs.  $T$  measured up to 1800 K on arc-melted specimens by [80MTNK] (curve 1), [72OKN] (3) and [64C] (4) as well as on sintered samples by [70FKWM] (2).



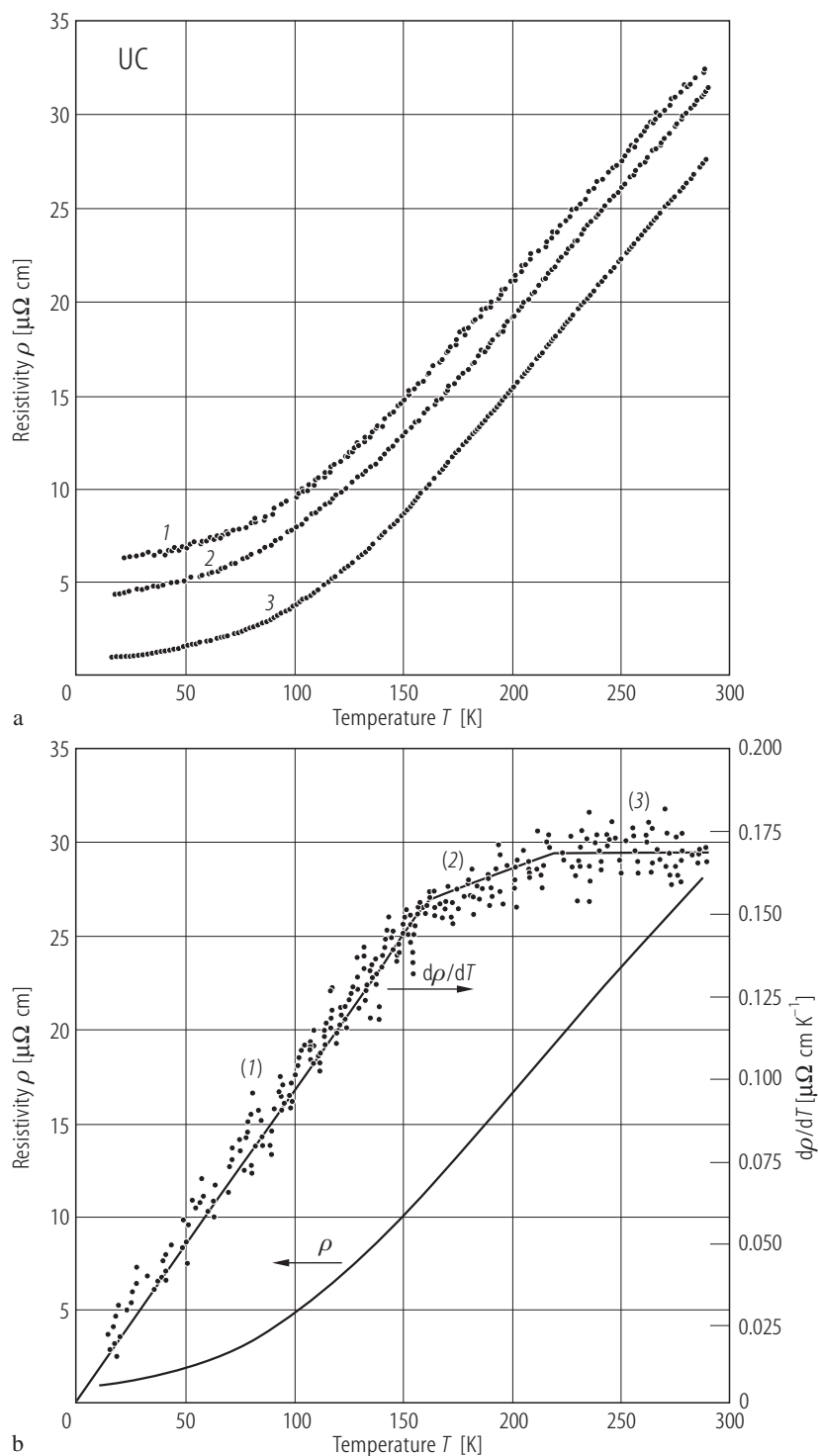


**Fig. 1.32.** UC s.c. **(a)** Electrical resistivity,  $\rho$ , vs.  $T$  for three samples, one polycrystalline (curve 1) and two single crystalline samples being "random" (without alignment to the crystalline axes, curve 2) and "aligned" along the [100] or [110] (not shown in the figure) axes [88MKY]. **(b)** Temperature dependence of  $\rho$  and its derivatives ( $d\rho(T)/dT$ ) for a [100] aligned, single-crystalline UC with slightly hyperstoichiometric composition [88MKY]. Note three regions: (1) Below 160 K,  $\rho(T) = a_1 T^2 + c_1$  ( $d\rho/dT = 2a_1 T$ ); (2)  $160 < T < 220$  K,  $\rho(T) = a_2 T^2 + b_2 T + c_2$ ; and (3) above 220 K,  $\rho(T) = b_3 T + c_3$ , ( $d\rho/dT = b_3$ ). Such a behaviour of  $\rho(T)$  is explained as being dominant by the electronic contribution at lower temperatures and by a phonon-type conduction at higher temperatures. For more explanations in terms of the influence of the vacancies in carbon and uranium on  $\rho(T)$  see [89MKYO].

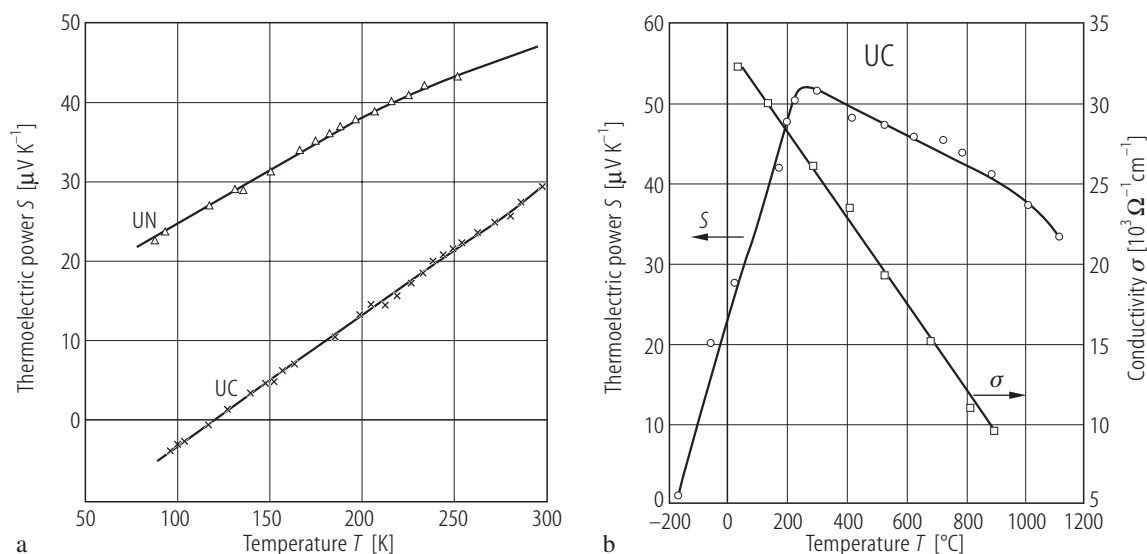


**Fig. I.35.** UC, UN. **(a)** The thermoelectric power,  $S$ , vs.  $T$  for polycrystalline UC and UN between 77 and 300 K [72OKN]. Also the Seebeck coefficient as a function of temperature for various compositions  $x$  for the solid solutions  $\text{UC}_{1-x}\text{N}_x$  was displayed in [72OKN], but not

shown here. **(b)** Thermoelectric power,  $S$ , and electrical conductivity,  $\sigma$ , as a function of temperature measured up to 1100 and 900  $^{\circ}\text{C}$ , respectively, on hot-pressed samples of UC [64WP].

For Fig. I.36 see next page

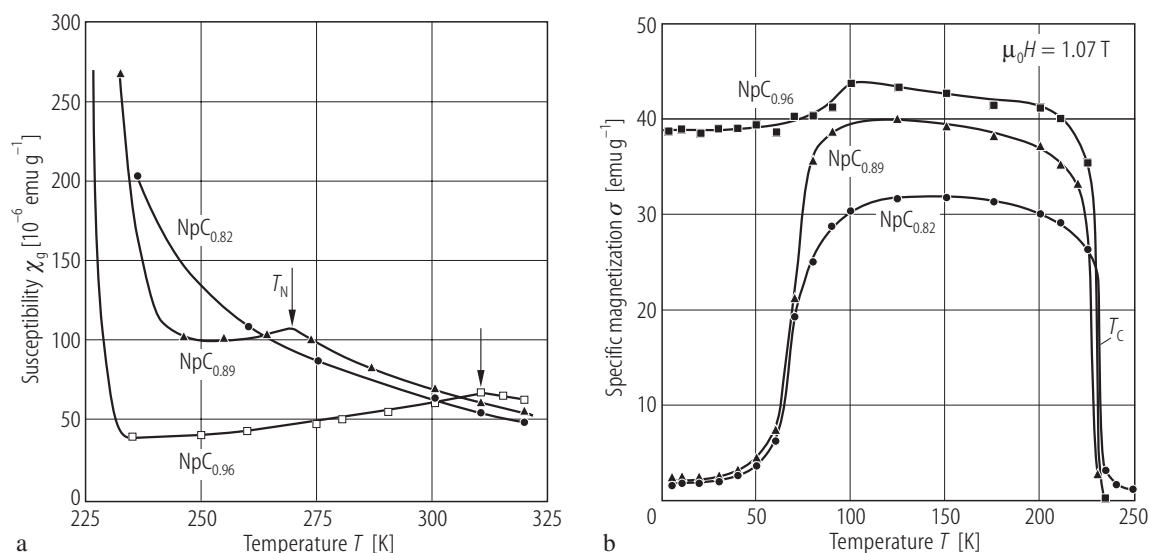


**Fig. I.37.**  $\text{NpC}_{1-x}$ . **(a)** Specific magnetic susceptibility  $\chi_g$  vs.  $T$  for substoichiometric neptunium monocarbides with different carbon concentrations:  $x = 0.04$ ,  $0.11$  and  $0.18$  measured between 225...350 K and **(b)** specific

magnetization,  $\sigma$ , vs.  $T$  below 250 K for the same compositions [71LMPL]. The curves were obtained by first cooling in a zero external magnetic field and then measured at 1.07 T.

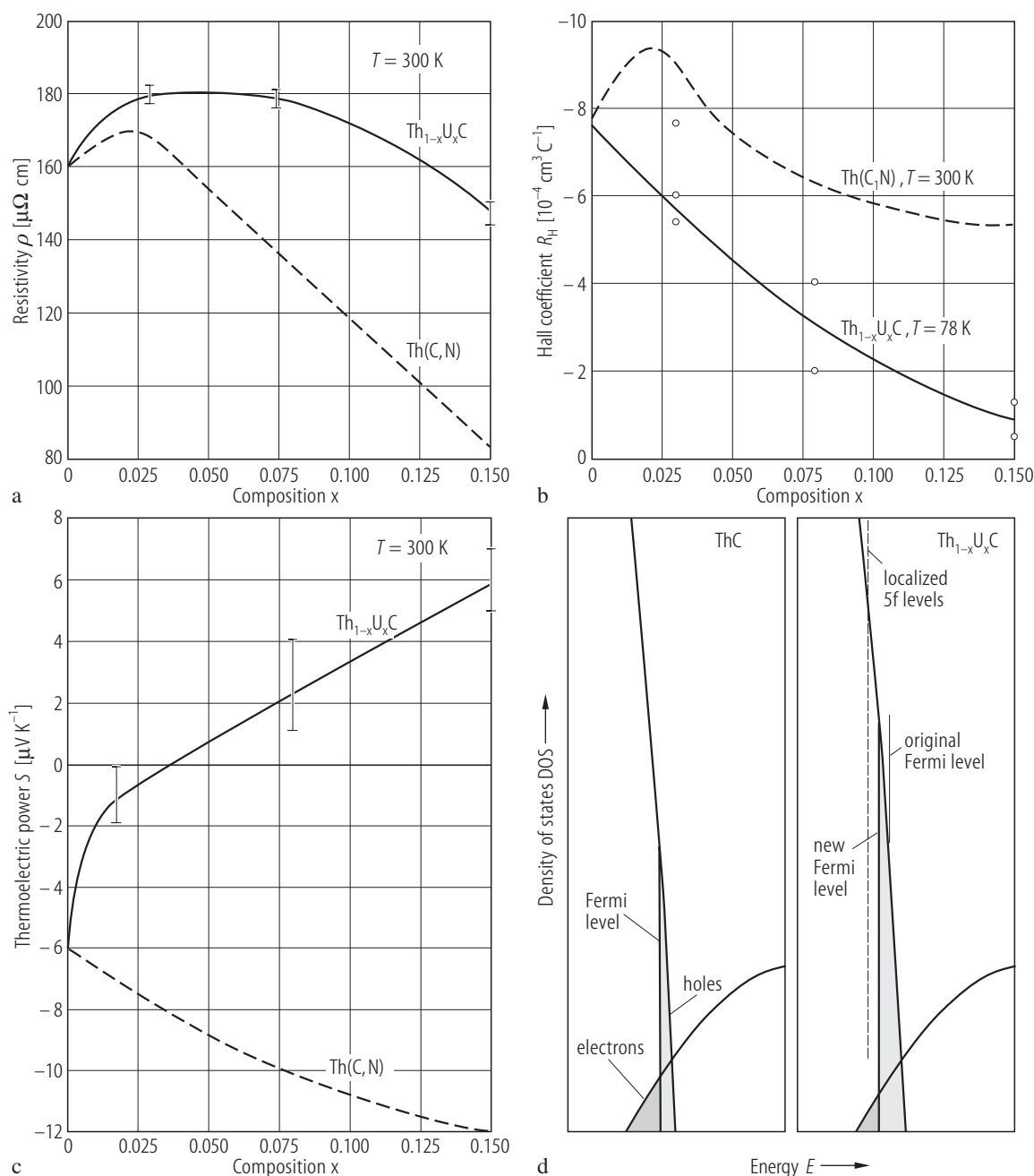


**Fig. 1.36.** (Th,U)C. **(a)** RT electrical resistivity  $\rho$ , corrected for sample porosity, as a function of uranium content up to 15 mol% (solid line) [69AA]. The dashed line represents data of [70AA] for thorium carbonitrides having the same valence electron concentration (VEC) as the thorium-uranium carbides (see also [68AA] and Fig. 377 in LBIII/19f2). **(b)** Hall coefficient  $R_H$  corrected for sample porosity, as a function of uranium content up to 15 mol% (open circles) [69AA]. The dashed line represents data for the same VEC for thorium carbonitrides [70AA].

**(c)** Thermoelectric power  $S$  vs. uranium content up to 15 mol % (solid line) [69AA]. The dashed line represents results for the same VEC for thorium carbonitrides [70AA]. **(d)** Schematic DOS as a function of energy based on the data presented in (a), (b), and (c) for ThC and (Th,U)C [69AA]. In addition, the two extra electrons donated by uranium (see 5f localized level) act as sinks for band electrons lowering  $E_F$  which results in an increased ratio of holes to electrons. This picture is opposite to that presented by [64BU], where  $E_F$  shifts up in energy.

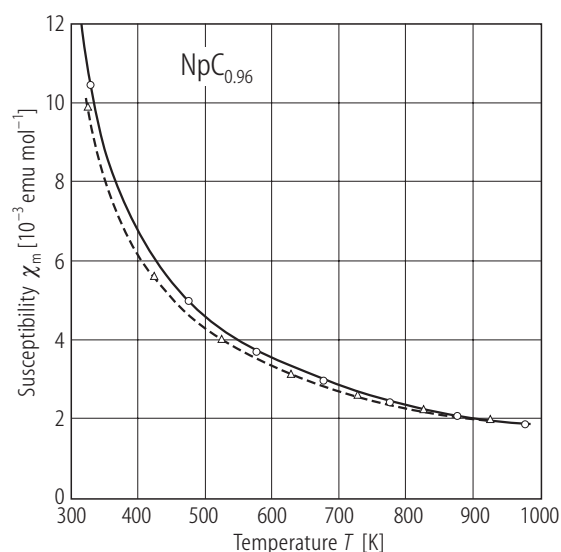


**Fig. I.38.**  $\text{NpC}_{1-x}$ . Molar magnetic susceptibility,  $\chi_m$ , vs. temperature,  $T$ , for a  $\text{NpC}_{0.96}$  sample [70CL]. Experimental values are represented by the solid curve (open circles) and theoretical values by the dashed curve (triangles). In calculations of  $\chi_m(T)$  for  $\text{NpC}$  ( $5f^3$ ), an unperturbative theory of  $J$ -mixing has been used [74CL]. The relevant parameters for the following interactions are: 1) Coulomb:  $E^1 = 3357.8 \text{ cm}^{-1}$ ,  $E^2 = 17.08 \text{ cm}^{-1}$ ,  $E^3 = 327.28 \text{ cm}^{-1}$ ; 2) spin-orbital:  $\zeta_{5f} = 2193.0 \text{ cm}^{-1}$  and crystal-electric field:  $A_4\langle r^4 \rangle = 2365.6 \text{ cm}^{-1}$  and  $A_6\langle r^6 \rangle = 10 \text{ cm}^{-1}$ .

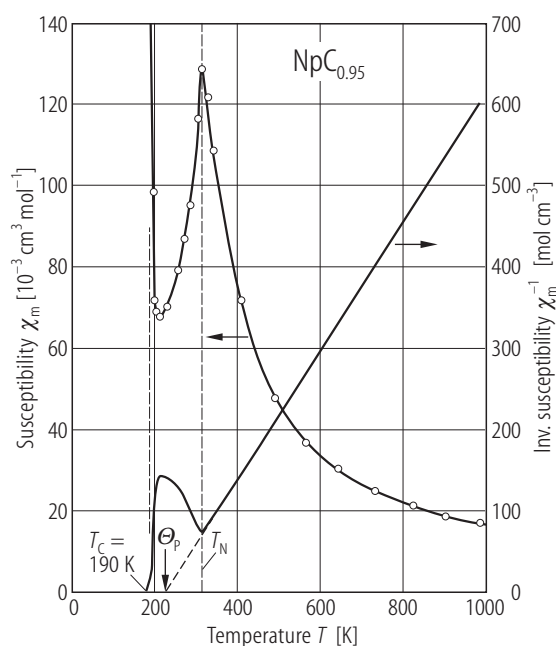


**Fig. I.39.**  $\text{NpC}_{1-x}$ . Molar magnetic susceptibility,  $\chi_m$ , (lhs) and inverse magnetic susceptibility,  $\chi_m^{-1}$ , (rhs) for  $\text{NpC}_{0.95}$  measured up to 1000 K [68DL]. The AF to F phase transition occurs at  $T_C = 190 \text{ K}$ .  $T_N = 317 \text{ K}$ ,  $p_{\text{eff}} = 2.13 \mu_B$ . Compare this behaviour with that of  $\text{NpC}_{0.96}$  ( $T_C = 225(5) \text{ K}$ ,  $T_N = 310(5) \text{ K}$ ) presented by [71LMPL]. (Also presented in LBIII/19f2, Fig. 394).

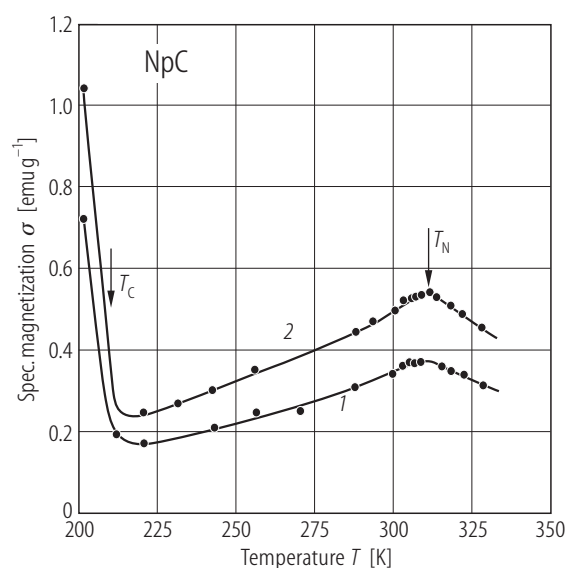


**Fig. I.40.**  $\text{NpC}$ . Specific magnetization,  $\sigma$ , vs. temperature,  $T$ , from 200 to 330 K measured at two magnetic fields: (1)  $H = 7.25 \text{ Oe}$  and (2)  $H = 10.28 \text{ Oe}$  [67RL].  $a_0 = 0.4994 \text{ nm}$ ,  $T_N = 310 \text{ K}$ ,  $p_s = 1.4 \mu_B$ . Between 310 and 350 K,  $p_{\text{eff}} = 3.0 \mu_B$ . This moment, but determined from  $\chi_m^{-1}$  vs.  $T$  up to 1000 K, is  $3.37 \mu_B$  (see Fig. I.39).

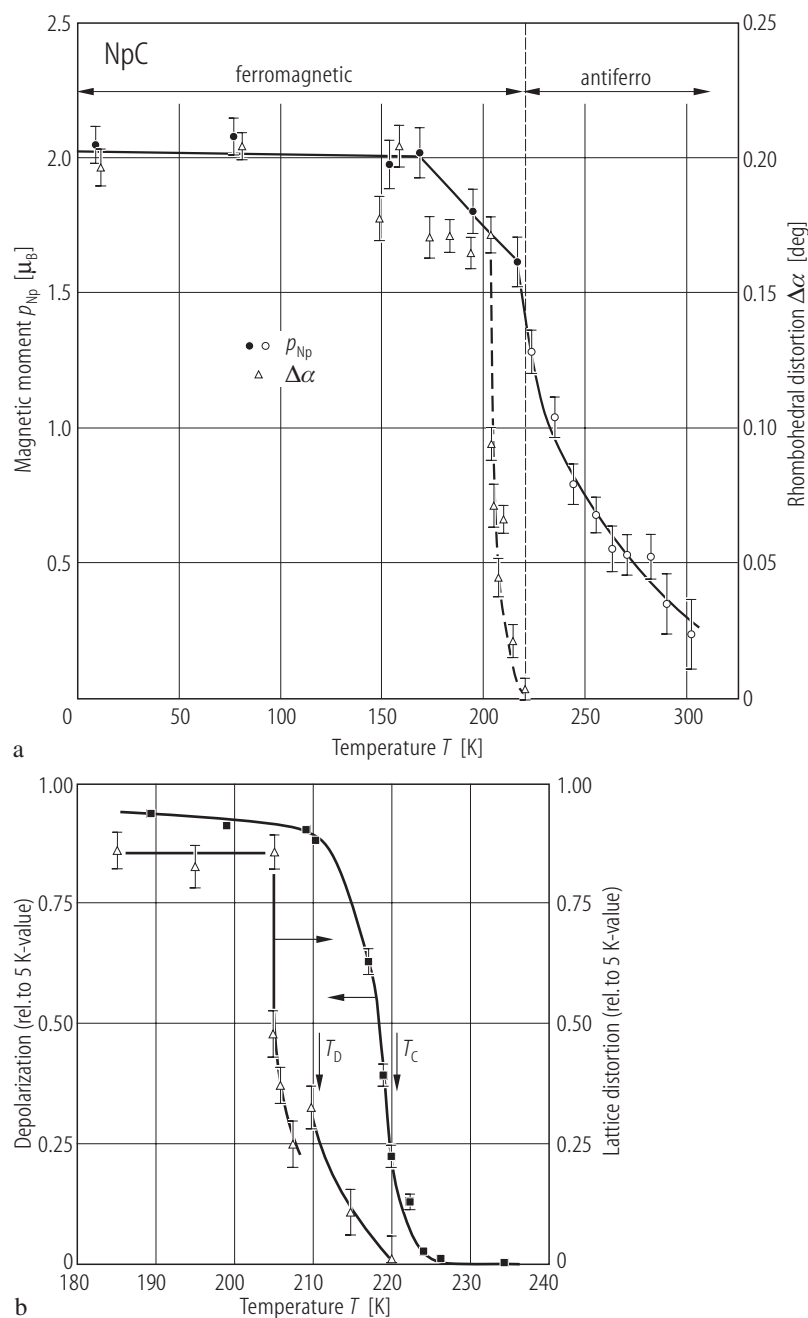
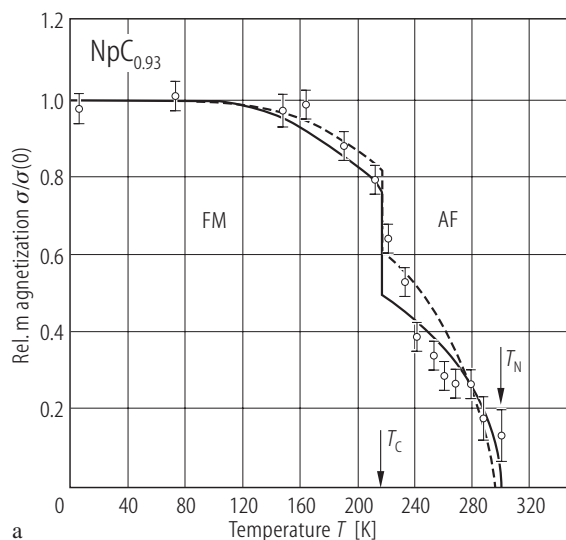
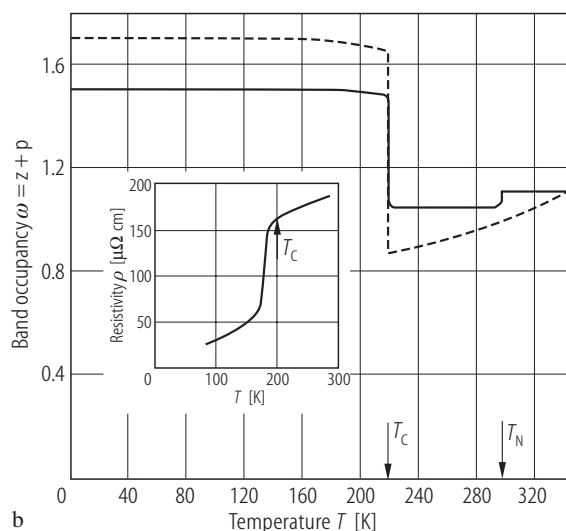


**Fig. I.41.** NpC. **(a)** The ordered magnetic moment,  $p_{\text{Np}}$ , (closed circles) taken from [69LHMA] and the rhombohedral distortion  $\Delta\alpha$  (open triangles) as a function of temperature [74LM]. Here the rhombohedral distortion is defined as an angle  $\Delta\alpha = -8/\sqrt{27} (c'-a')/a'$ , where the distances  $c'$  and  $a'$  are measured parallel and perpendicular to the trigonal axis, respectively (see Table 9). Note that the onset of the rhombohedral distortion at  $T_C$  appears to be almost first-order kind in nature, but it does not lead to an appreciable hysteresis. **(b)** The ratio of the size of

depolarization of polarized neutrons transmitted (closed squares) to the lattice distortion (open triangles) around the Curie temperature  $T_C$  ( $= 220 \dots 223$  K) [74LM]. It should be emphasized that the distortion temperature  $T_D$  and  $T_C$  show about 10 K difference, while in all other actinide compounds  $T_D \approx T_C$ . In the type I antiferromagnetic phase range (220...350 K) the unit cell is cubic and no distortion is detected with an accuracy of  $|(c'-a')/a'| \leq 5 \cdot 10^{-4}$  was observed at 5 K. (See also LBIII/19f2, Fig. 396).

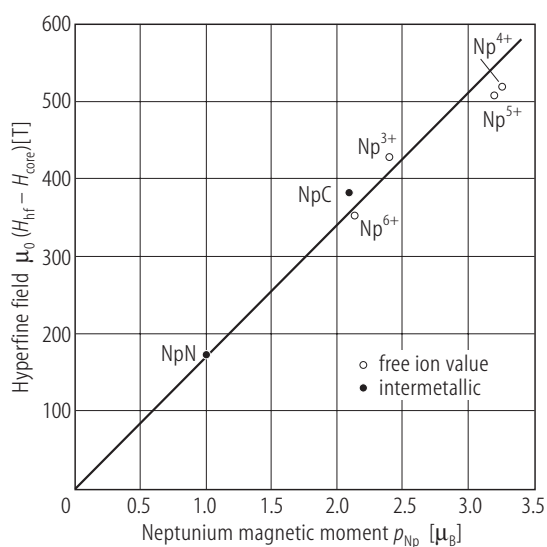


a

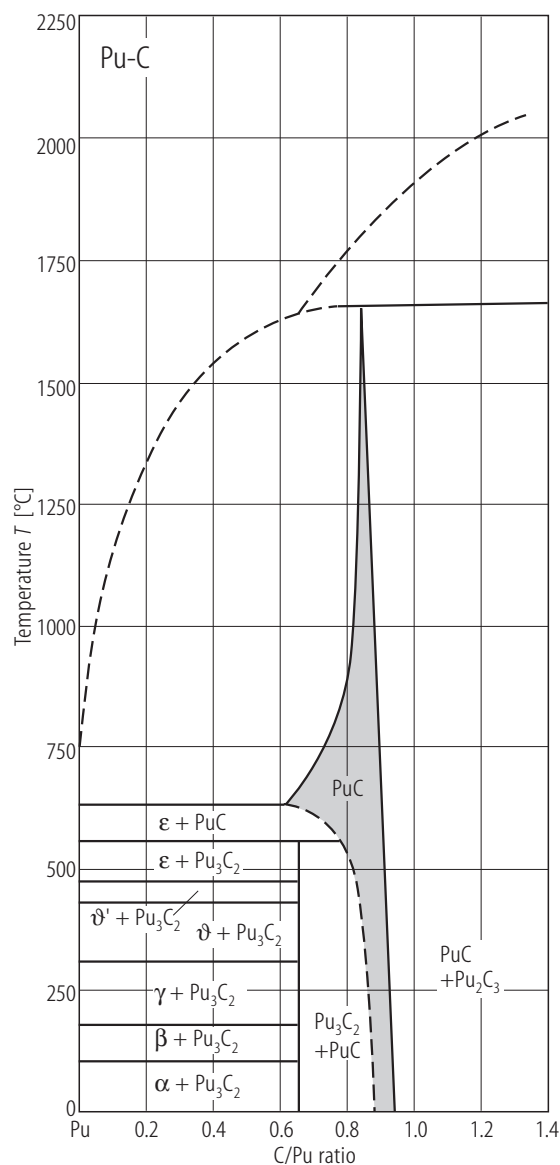


b

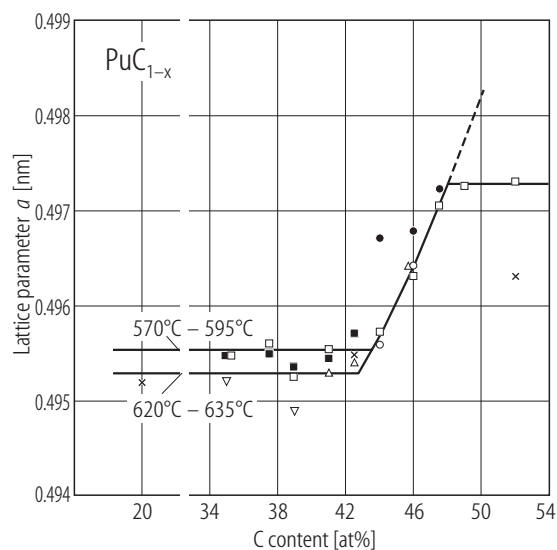
**Fig. I.42.**  $\text{NpC}_{1-x}$ , ( $x = 0.07$ ). Relative sublattice magnetization,  $\sigma/\sigma(0)$ , (open circles, data from [69LHMA]), **(a)** (upper panel) and conduction electrons,  $\omega (= z+p)$ , **(b)** (lower panel) as functions of temperature,  $T$ , compared to the results of the electron-delocalization theory (solid and dashed lines) (see also for explanation Fig. R.13a) [74RE]. The two different theoretical approaches are due to using two different values of fitting parameters (see the original paper). Insert: The  $\rho$  vs  $T$  curve around  $T_C$  (taken from [72B]) correlates well with the observed jump in  $\rho(T)$  at  $T_C$ , if one assumes that  $\rho(T)$  is roughly proportional to the change in band occupancy,  $\omega$ .



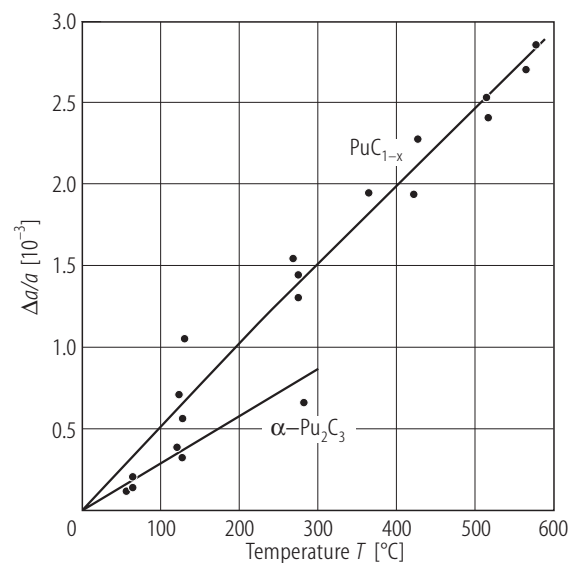
**Fig. I.43.**  $\text{NpC}$ ,  $\text{NpN}$ . A relationship between magnetic hyperfine field content  $H_{\text{orb}} (= H_{\text{hf}} - H_{\text{core}})$  and the ordered magnetic moments  $p_{\text{Np}}$  in  $\text{NpC}$  ( $2.1 \mu_B$ ) and  $\text{NpN}$  ( $\sim 1 \mu_B$ ) as well as in the free ions of  $\text{Np}^{3+}$  ( $2.40 \mu_B$ ),  $\text{Np}^{4+}$  ( $3.27 \mu_B$ ),  $\text{Np}^{5+}$  ( $3.20 \mu_B$ ) and  $\text{Np}^{6+}$  ( $2.14 \mu_B$ ) [72DK]. Core polarization  $H_{\text{core}}$  for the actinide ions is usually large and cannot be ignored. It is assumed independent of  $p_{\text{Np}}$  and was calculated (see the text of original paper).



**Fig. I.44.**  $\text{PuC}_{1-x}$ . A part of C–Pu phase diagram compiled on the basis of data from the literature [86H]. Note that monocarbide occurs only hypostoichiometrically and has a homogeneous region (shaded area). The symbols present the two-phase regions containing different Pu phases.

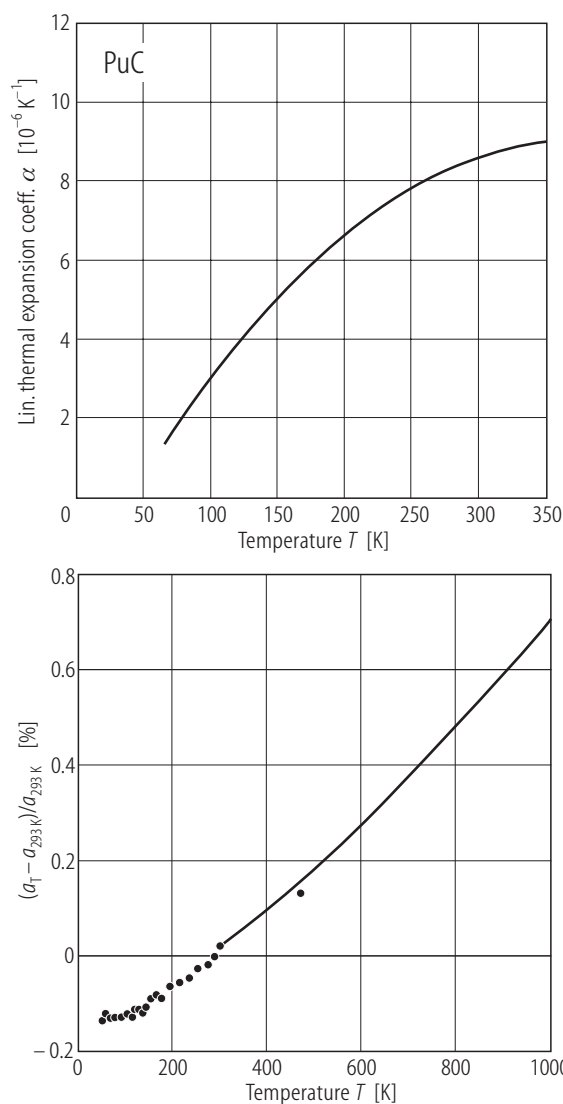


**Fig. I.45.**  $\text{PuC}_{1-x}$ . Lattice parameter,  $a$ , vs. composition in at. % [63RNM]. Note that this compound exists in a wide composition range below stoichiometric composition. The symbols mean that the samples were homogenized at different temperatures from 400 to 1500°C. The solid lines correspond to the temperatures given in the figure.



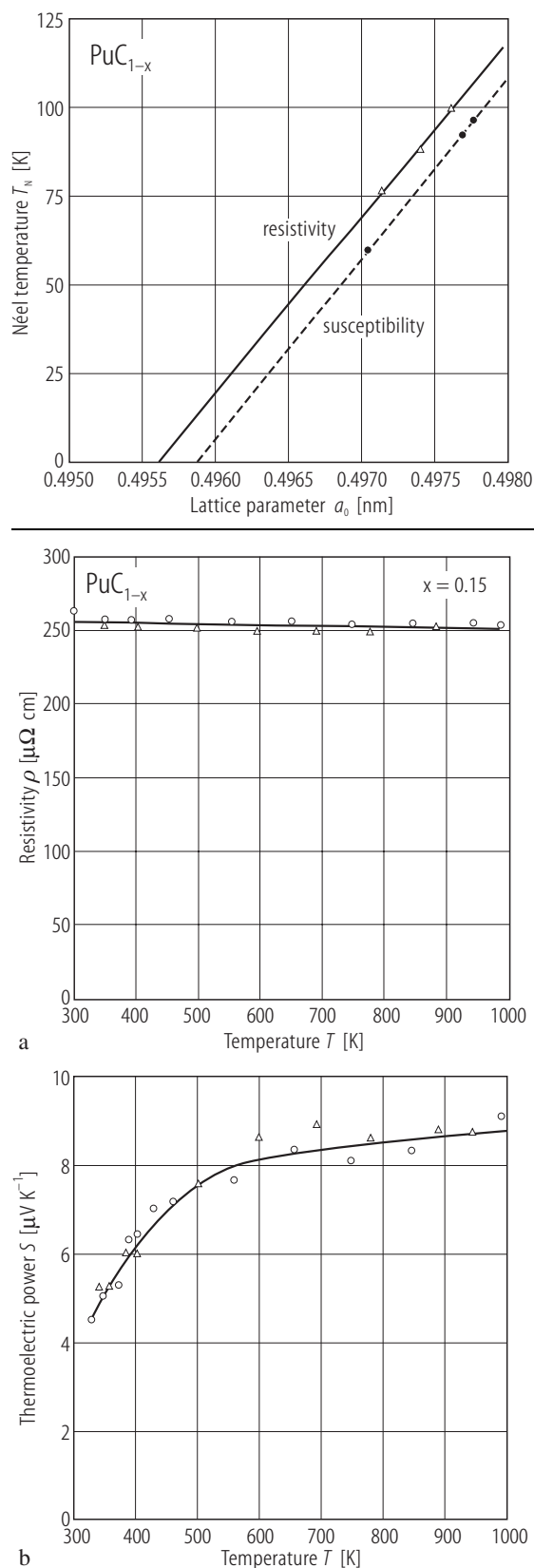
**Fig. I.46.**  $\text{PuC}_{1-x}$ . The change in the lattice parameters,  $\Delta a/a$ , vs. temperature,  $T$ , (up to 600°C) compared to that for  $\alpha\text{-Pu}_2\text{C}_3$  (up to 300°C) [64BSC].

**Fig. I.48.**  $\text{PuC}_{1-x}$ ,  $0.04 \leq x \leq 0.12$ . The Néel temperature,  $T_N$ , determined from the temperature variation of the resistivity,  $\rho(T)$ , and magnetic susceptibility,  $\chi(T)$ , vs. lattice parameter,  $a_0$ , for the plutonium carbides deficient in carbon [65LCP]. See there also the magnetic characteristics for these carbides.



**Fig. I.47.** PuC. Linear thermal expansion coefficient,  $\alpha$ , and instantaneous coefficient of thermal linear expansion,  $(a_T - a_{293 \text{ K}})/a_{293 \text{ K}}$ , vs. temperature [79BDM].

**Fig. I.50.**  $\text{PuC}_{1-x}$ . (a) Electrical resistivity,  $\rho$ , and (b) thermoelectric power,  $S$ , as a function of temperature,  $T$ , in the range: 300...1000 K measured for a carbon-deficient, arc-melted sample with  $x = 0.15$ .  $\rho(300) = 257 \text{ } \mu\Omega\text{cm}$ ,  $S(300 \text{ K}) = 5 \text{ } \mu\text{V/K}$  [67KM1].





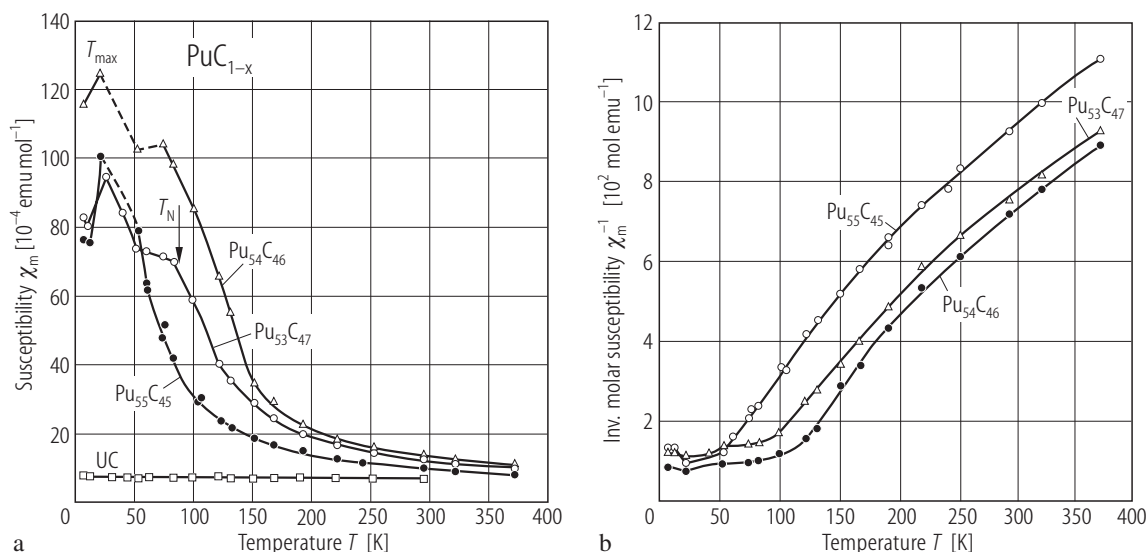


**Fig. 1.49.** PuC<sub>1-x</sub>. **(a)** Molar magnetic susceptibility,  $\chi_m$ , vs. temperature,  $T$ , for three compositions with  $x = 0.18, 0.15$  and  $0.11$  compared to that of UC. Due to self-radiation damage all samples showed time-dependent magnetizations below 50 K [67LNRM]. **(b)** Inverse molar magnetic susceptibility,  $\chi_m^{-1}$ , vs. temperature,  $T$ , for the above compositions [67LNRM]. All three samples showed a marked deviation from C-W behaviour and a susceptibility maximum at 20 K. The high-temperature susceptibility of

PuC<sub>0.78</sub> (not shown) follows a MCW law with  $\chi_0 = 300 \cdot 10^{-6} \text{ emu/F.U.}$ ,  $\Theta_p = -20 \text{ K}$  and  $p_{\text{eff}} = 2.37 \mu_B/\text{F.U.}$  [74LA]. The reciprocal molar susceptibility,  $\chi_m^{-1}$  vs. temperature,  $T$ , for PuC<sub>0.78</sub> ( $a_0 = 0.4956 \text{ nm}$ ) was shown in LBIII/19f2 in Fig. 398 [74LA]. Neutron diffraction experiment of [70GALN] showed for  $x = 0.18$  ( $a_0 = 0.4969 \text{ nm}$ ) a ferromagnetic transition of the first-order kind at  $T_N \approx 100 \text{ K}$ .  $p_0$  (at 20 K)  $\approx 0.8 \mu_B/\text{Pu at.}$

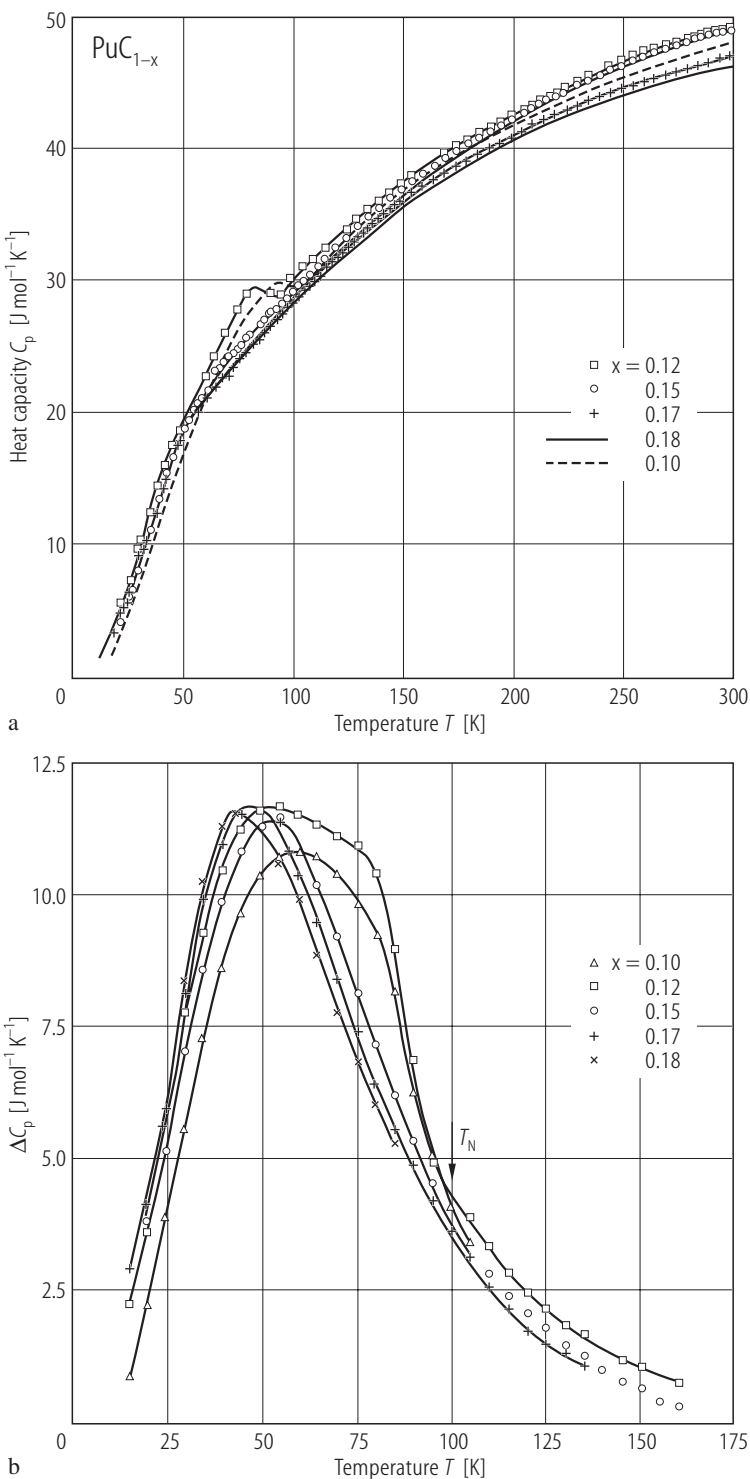


**Fig. 1.51.** PuC<sub>1-x</sub>. **(a)** Heat capacity,  $C_p$ , vs. temperature,  $T$ , for three compositions of PuC<sub>1-x</sub>:  $x = 0.17$ ,  $0.15$  and  $0.12$  (symbols) [77HHL]. The data for  $x = 0.18$  and  $0.10$  (solid and dashed lines) are taken from [76MHHL]. The heat capacity parameters are presented in the Table below:

	$\gamma(0)$ [mJ/K <sup>2</sup> mol]	$\Theta_D$ [K]
PuC <sub>0.80</sub> <sup>*</sup>	13.5	395
PuC <sub>0.83</sub>	15.2	400
PuC <sub>0.85</sub> <sup>*</sup>	19.8	405
PuC <sub>0.90</sub> <sup>*</sup>	13.9	415

<sup>\*</sup>) Ref. [76MHHL].  
**(b)** Difference  $\Delta C_p$  between measured  $C_p$  and calculated (Debye+electronic) curves vs. temperature,  $T$ , [76HHL]. Note that the transition mechanism changes from non-cooperative to cooperative with increasing carbon concentration. Heat capacity  $C_p$  vs. temperature,  $T$ , for PuC<sub>0.80</sub> is also shown in LBIII/19f2 in Fig. 400 [80HLM]. Note that around  $T_N$  ( $=45$  K) a superimposed anomaly on the usual sigmoid temperature dependence occurs. The antiferromagnetic transition is also seen in the  $\rho(T)$  [65LCP] and  $\chi(T)$  curves [67LNRM].